Chemical Engineering Journal 521 (2025) 166038

Contents lists available at ScienceDirect

Chemical Engineering Journal

journal homepage: www.elsevier.com/locate/cej

Dual injection in a CO_2 microwave plasma: Exploring post-plasma quenching with CH_4 and comparison with DRM

E.R. Mercer [a,b,c,*], M. Albrechts [a,b,c], R. De Meyer [a,b,c,d,e], I. Fedirchyk [a,b,c], E. Morais [a,b,c], S. Bals [d,e], A. Bogaerts [a,b,c]

[a] Research group PLASMANT, Department of Chemistry, University of Antwerp, Belgium
[b] Center of Excellence PLASMA, University of Antwerp, Belgium
[c] Electrification Institute, University of Antwerp, Belgium
[d] Research group EMAT, Department of Physics, University of Antwerp, Belgium
[e] NANOlight Center of Excellence, University of Antwerp, Belgium

ARTICLE INFO

Keywords:
Microwave plasma
Dual injection
CO_2 conversion
Dry reforming of methane (DRM)
CCU technology
Post-plasma quenching
Reactive quenching

ABSTRACT

We investigated dual injection in a 2.45 GHz CO_2 microwave plasma, where CH_4 is injected into the afterglow region as a novel approach to utilize the high post-plasma temperatures for additional chemistry with reactive quenching. The experiments were conducted at various pressures, powers, and CO_2:CH_4 ratios. We find that dual injection effectively enhances absolute CO_2 conversion, with a maximum reported value of ~55 % at 1250 W, 500 mbar, and a CO_2:CH_4 ratio of 7:7 slm. Furthermore, we compare our dual injection method with conventional (admixing) dry reforming of methane (DRM), using a comprehensive analysis of gaseous and liquid products, as well as carbon structure and morphology. The latter exhibits an unusual fused amorphous structure, distinctly formed under fast cooling conditions. Using chemical kinetics modeling, we identify important kinetic pathways, explaining the enhanced CO_2 conversion by the removal of O atoms and O_2 molecules, which prevents their participation in recombination reactions, while supplying H atoms upon CH_4 dissociation. This results in the reverse water-gas shift reaction, which lowers the syngas ratios compared to conventional DRM. Nonetheless, the model predicts that increasing the specific energy input (*SEI*), or the amount of power applied to the chemistry in a single pass through the reactor, may achieve more competitive syngas ratios. Our findings represent an advancement toward precise control of microwave-based plasma chemistry.

1. Introduction

The urgency to address climate change has intensified efforts to transform a usual 'waste product', such as carbon dioxide (CO_2), from an environmental liability into a valuable chemical resource. While renewable electricity generation has seen remarkable growth in the past few years [1], with solar and wind becoming increasingly cost-competitive, the challenge of decarbonizing the industrial sector remains particularly daunting. A prime example lies in the chemical manufacturing sector, which has been presented with a significant challenge for achieving global emission reduction targets. The chemical sector is responsible for being the largest industrial energy consumer and the third largest industry subsector for direct CO_2 emissions, and must achieve a 75 % reduction by 2050 to align with the goals outlined in the Paris Agreement [2]. Among various Carbon Capture and Utilization (CCU) pathways, plasma-based conversion represents a particularly promising approach for coupling renewable electricity to chemical production. As renewable energy increasingly penetrates global power infrastructures, technologies capable of absorbing an intermittent power supply, such as plasma technology, while producing valuable chemicals are becoming critical components of a circular carbon economy.

Plasma-based gas conversion, particularly using microwave (MW) plasma, has garnered significant attention due to its unique advantages of rapid response to power fluctuations, electrodeless operation, and potential for high energy efficiency [3–5]. The process enables the dissociation of CO_2 into carbon monoxide (CO) using electricity from renewable sources, effectively transforming intermittent energy into chemical precursors for liquid fuels [3], such as CO feedstock for Fischer-Tropsch synthesis [6], of which the products can be readily

* Corresponding author at: University of Antwerp, Campus Groenenborger, Gebouw W, Groenenborgerlaan 171, 2020, Antwerpen, Belgium.
E-mail address: Elizabeth.Mercer@UAntwerpen.be (E.R. Mercer).

https://doi.org/10.1016/j.cej.2025.166038
Received 23 March 2025; Received in revised form 28 June 2025; Accepted 14 July 2025
Available online 24 July 2025

stored and utilized within our existing infrastructure. Furthermore, MW plasma reactors can be designed for deployment at local or regional scales, minimizing the CO_2 footprint associated with transporting the key chemicals that underpin society. While results from MW plasma-based CO_2 conversion are encouraging, the energy efficiency remains highly dependent on specific operating parameters and reactor design considerations.

Consequently, research efforts have increasingly focused on optimizing the dissociation of CO_2 to CO using MW plasma systems to advance this promising technology [7–16], with much emphasis on progressing the community's understanding of what limits high conversion and energy efficiency [4,12,13,15,17–21]. These recent studies have highlighted the importance of post-plasma quenching in CO_2 plasma to maximize conversion and energy efficiency, with many experimental studies focused on rapidly decreasing the extreme temperatures measured in the afterglow region (typically $T >> 1500$ K) by enhanced mixing of cool periphery flows and the hot reactive volume using nozzles [8–10,14,20,22]. The goal of such strategies is to reduce 'burn back', typically observed as a blue afterglow in CO_2 MW plasmas, resulting from the chemiluminescent recombination of CO + O to CO_2 [23]; however, such high temperatures observed in the downstream afterglow region have the potential to transfer the exergy into additional chemistry using methods of reactive quenching (also known as chemical trapping) [12,24–26]. Moreover, the removal of O atoms and O_2 molecules through reactive quenching in the afterglow of CO_2 plasma has been found to enhance the retainment of CO [19,27–30].

One effective example of reactive quenching is placing a carbon bed in the afterglow region of CO_2 plasmas [28–31], which has been shown to significantly improve the yield of CO by removing O atoms and O_2 molecules while reducing the overall energy cost. *Girard-Sahun* et al. [28] showed that a carbon bed placed directly after a Gliding Arc Plasmatron (GAP) reactor enhances the CO_2 conversion while achieving an oxygen-free effluent. This research successfully demonstrated how eliminating O atoms and O_2 molecules in the post-plasma gas mixture not only enhances CO output, but also eliminates the need for one of the most expensive separation steps required for industrialization [32] while simultaneously lowering the energy cost of the conversion process. Follow-up research by *Biondo* et al. [29] revealed that reducing the distance between reactor outlet and carbon bed further enhances performance by facilitating direct interaction between the carbon pellets and the reactive species in the afterglow. Moreover, *O'Modhrain* et al. demonstrated the effects of bed size and insulation, noting the influence of higher post-plasma temperature on conversion, and included a detailed study on the positive effects associated with bed insulation and preheating the carbon prior to entry into the bed, highlighting essential aspects of thermal management in plasma systems [30]. This emphasizes the importance of reactive quenching and thermal management in controlling recombination in the post-plasma region.

The literature for post-plasma reactive quenching using a secondary gas injection (i.e., via dual injection) is limited. A study by *Chekmarev* et al. [33] demonstrated a threefold increase in CO_2 conversion by injecting nitrogen (N_2) as a quenching gas in the post-plasma region. Although the authors reported that the dissociation of N_2 was minor, they successfully showed an increase in conversion and energy efficiency as a function of the secondary injection of N_2 flow rates. Another study by *Chekmarev* et al. [34] showed that using argon (Ar) as a post-plasma quenching agent was also successful at reducing recombination, with observed reduction of the characteristic flame band afterglow from recombination to CO_2, as well as an accompanying enhancement in conversion [23]. These examples highlight the importance of understanding the role of secondary injection quenching in plasma-based chemical conversion.

As research has demonstrated, controlled manipulation of the post-plasma environment by introducing improved mixing, thermal management, and oxygen scavenging in the CO_2 afterglow region can significantly improve conversion [8–10,14,20,28–30,33,35], helping to optimize process performance in plasma systems. This raises the question of whether the strategy of introducing a reactive quenching gas, such as an oxygen scavenger like methane (CH_4), shows the same promise for enhancing reactor performance. Experimental and modeling investigations by *Aerts* et al. [36] reveal that in-situ scavenging of O atoms and O_2 molecules via a hydrogen source (e.g., CH_4), provides an oxygen-free effluent mixture that can be more easily separated using existing technologies [32,37,38]. When CO_2 is combined with CH_4, the reaction produces a mixture of CO and hydrogen (H_2), which is a versatile precursor for fuels and chemicals, known as synthesis gas (syngas). This reaction is widely known as dry reforming of methane (DRM); however, controlling this process efficiently in plasma systems presents several challenges, such as controlling the syngas ratio and dealing with solid carbon formation at higher CH_4 fractions [39–49].

The difficulty in controlling the produced syngas ratio (i.e., H_2:CO) presents a critical limitation when admixing CO_2 and CH_4 in plasma-based DRM. This is because, in ideal DRM, the stoichiometric reaction yields a syngas ratio of 1; therefore, to achieve higher syngas ratios, e.g., around 2, which is required for methanol synthesis or the Fischer-Tropsch process [6], significantly more CH_4 must be converted over CO_2. However, when admixing CO_2 and CH_4, increasing the CH_4 fraction reduces the absolute conversion of this reactant [40,42], as well as increases solid carbon formation. For instance, *Kelly* et al. [42] reported energy costs as low as 2.8 eV/molecule for MW plasma-based DRM, with CO_2 and CH_4 conversions of 49 % and 67 %, respectively. However, the authors reported significant plasma instability at CH_4 fractions exceeding 45 %, attributed to solid carbon formation in the plasma region [42]. The syngas ratio in the product stream remained at $\lesssim$1, consistent with other reports in literature [9,44]. The formation of solid carbon in plasma-based DRM creates operational instability, affecting power coupling and destabilizing the plasma [40,42,45,47,49]. This carbon formation not only reduces process efficiency but also requires frequent maintenance of reactor components. *Wanten* et al. [47] performed experiments in an atmospheric pressure glow discharge (APGD), and reported that increasing the CH_4 fraction led to an increasingly unstable plasma due to the formation of solid carbon. This negatively affected the conversion and reactor performance in general and limited their experiments to CH_4 fractions $<$35 % [47]. This is particularly relevant in MW plasma-based DRM, as carbon particles formed during the reaction interact with the MW field, in turn destabilizing the discharge [40,42,50].

Several efforts to mitigate carbon formation in plasma-based DRM have been reported. *Biondo* et al. [40] showed that reverse vortex flow configurations can successfully suppress carbon formation at reduced pressures, suggesting the flow typology plays a critical role in carbon nucleation in MW plasmas [51,52]. *Maerivoet* et al. [49] demonstrated that the addition of O_2 to DRM (so-called OCRM) in an APGD resulted in the oxidation of solid carbon, allowing for more stable conditions; however, the results also revealed a higher selectivity to water (H_2O). In another APGD experiment, *Wanten* et al. [46] suppressed soot formation by admixing H_2O vapor to the reactive gas stream (in so-called bi-reforming, BRM), both enhancing plasma stability and increasing syngas ratios.

In the present work, we seek to mitigate the instability attributed to high CH_4 fractions and the resulting solid carbon formation by injecting CH_4 into the post-plasma region as a reactive quenching agent. An example of post-plasma CH_4 injection in literature was conducted by *Cho* et al. [41], where the authors ran experiments in a system utilizing dual injection for DRM with a 7:7 slm, CO_2:CH_4 ratio in a 2.45 GHz MW reactor. The study explored a two-phase system: within the resonance chamber, a CO_2 plasma was first generated utilizing a double helix injection at atmospheric pressure, followed by an injection of CH_4 at the start of an insulated stainless steel reforming reaction chamber [41]. The novel double-helix type plasma generator from this work reported conversion of ~91 % and energy efficiency of ~67 %, serving as an example of an extended reaction chamber, with two processes in series.

This contrasts with the system we propose, which uses direct post-plasma reactive quenching with the goal of reducing the post-plasma temperatures quickly to mitigate recombination reactions.

In our study, we introduce dual injection in a MW CO_2 plasma by injecting CH_4 into the high-temperature post-plasma region as a reactive quenching agent. Our experimental results are supported by modeling [24], which further investigates the reaction pathways. This configuration leverages the thermal energy of the plasma afterglow ($T > >$ 1500 K). We hypothesize that CH_4 will act as an effective quenching agent for O atoms and O_2 molecules generated in the primary CO_2 plasma, enhancing CO_2 conversion by suppressing CO recombination back to CO_2.

Our research aims to understand how this approach measures against pure CO_2 conversion. Furthermore, by enabling the treatment of larger CH_4 fractions (without plasma destabilization by carbon deposition), we also aim to determine how this might be beneficial in a DRM context, in relation to the syngas ratio, process stability, energy cost, and product selectivity compared to conventional (admixing) DRM. In this respect, we also investigate the liquid byproducts and solid carbon formation. We gain deeper insights into the experimental results by using a 0D chemical kinetics model designed to investigate the post-plasma reactions in a dual injection system. The model examines the mixing of the thermal CO_2 plasma effluent with cold CH_4 injection in the post-plasma region. By combining experiments and modeling, we seek to advance the practical implementation of these technologies for CO_2 utilization, representing a step toward more precise control of plasma chemistry, and investigating new pathways for the selective production of fuels and chemicals from greenhouse gases.

2. Methods

2.1. Experimental setup

As shown in Fig. 1, the MW plasma reactor is powered by a custom-designed 2.45 GHz solid-state source composed of a collection of LDMOS power amplifiers with a rated efficiency of ~54 % (LDMOS PAs, right

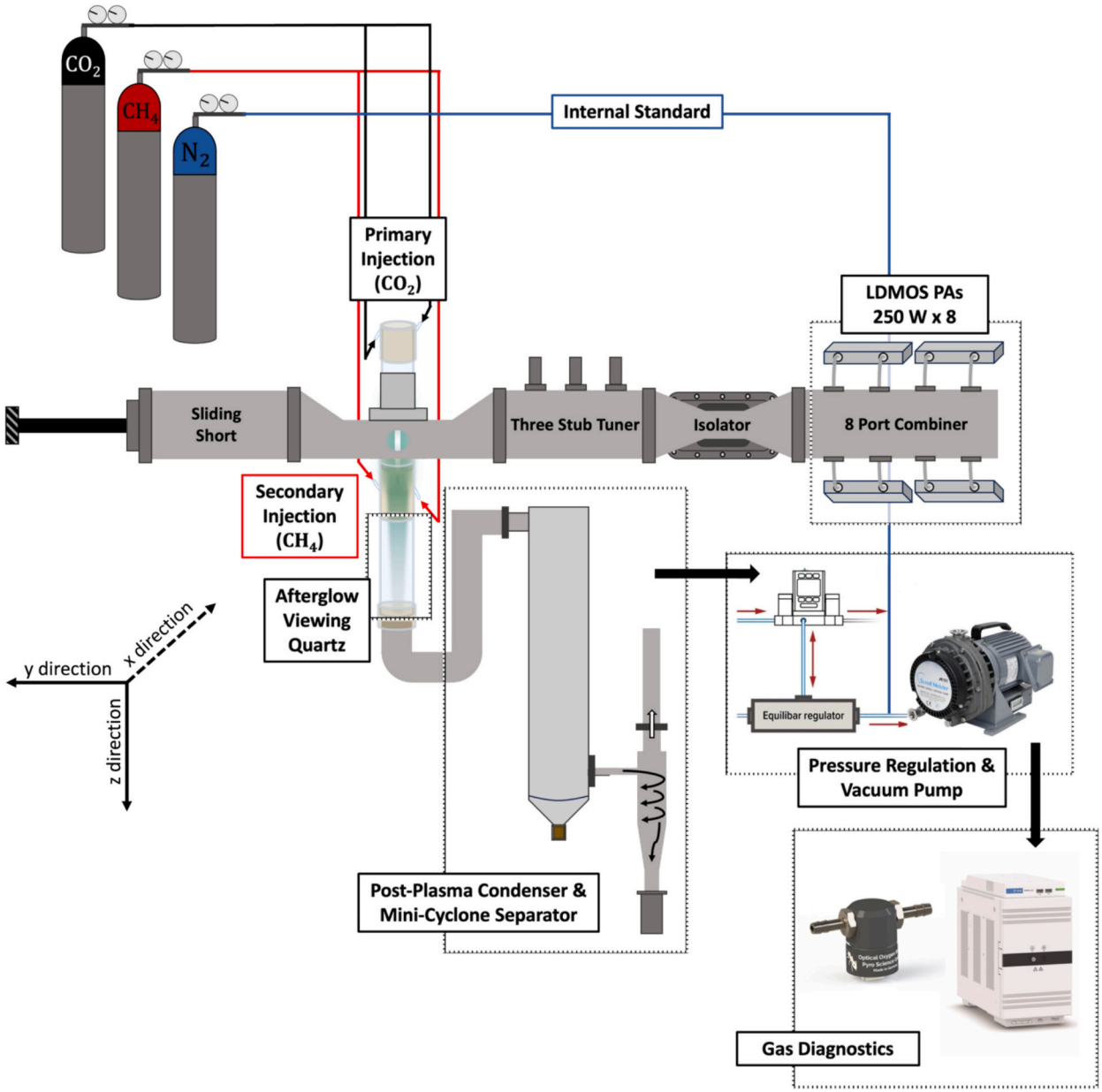

Fig. 1. Overview of the experimental setup.

side of Fig. 1) from which the output is combined in a specialized 8-port WR340 combiner waveguide, which is protected from reflected power by an isolator. The absorbed and reflected power (< 5 % for all results reported) were measured using the Homer series auto-tuner from S-TEAM labs. Together, the auto-tuner, impedance analyzer, and adjustable short tune the electric field to optimal conditions for electrical breakdown and to sustain the plasma. The tapered resonance chamber is intersected perpendicularly by a 16 mm inner diameter quartz tube, where the CO_2 plasma is formed as a surface-wave discharge. Directly after the plasma, CH_4 is injected into the afterglow region, which was monitored via the 'afterglow viewing quartz' to observe carbon formation.

As shown in Fig. 1, the product stream is fed into a post-plasma condenser, which collects the liquid products, analyzed using a series of diagnostic techniques outlined in *Supporting Information* (*SI*), *S1.1*. The cooled gas then moves to a miniature cyclone separator, which was designed to collect carbon particles down to 1 μm with 95 % efficiency [53]. The deposited carbon in the post-plasma region and cyclone separator is analyzed using two methods, scanning electron microscopy (SEM) and transmission electron microscopy (TEM) [42]. Additional information on the carbon characterization can be found in *SI, S1.2*.

A zoomed-in image of the injection setup is shown in Fig. 2, where the primary injection of the reactant gas (CO_2) is fed through the quartz discharge tube via a helical swirl inlet, at the right of Fig. 2. Upon ignition at subatmospheric pressure, a surface-wave sustained mode is generated, with an axially elongated warm plasma filament located in the center of the quartz tube, isolated from the tube walls by the vortex generated from the swirl inlet. Within the resonance chamber, optical emission spectroscopy (OES) is performed to analyze the spectrum generated by the plasma using an Ocean Insight mini spectrometer (HR-4UVV250–5) equipped with a solarization-resistant fiber with a diameter of 400 μm (QP400–2-SR) and cosine corrector with Spectralon diffusing material (CC-3-UV-S). Additional information on the optical techniques is available in *SI, S1.3*. A secondary counter-flow tangential injection of CH_4 with 1 mm inlets is initiated in the afterglow region, 5 cm from the waveguide, where temperatures exceed 1500 K (see *SI, S1.4,* for a detailed schematic of the secondary injection housing). The afterglow is viewed through a secondary quartz tube placed after the secondary injection housing, where we were able to observe irradiation from solid carbon (forming within the post-plasma) and any deposits on the quartz tube wall in real time. A thermocouple placed ~200 mm downstream measures the post-secondary injection temperature.

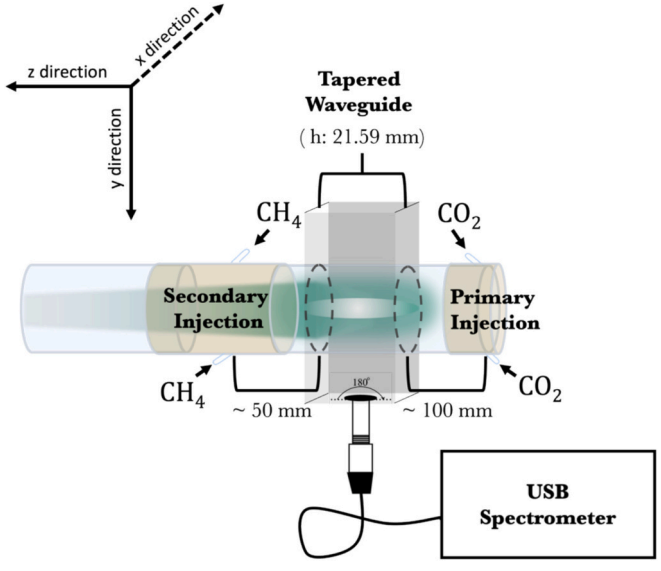

Fig. 2. Schematic view of the dual injection system with optical emission spectroscopy.

An internal standard, used to determine the expansion coefficient in order to correctly calculate the performance metrics [54], is introduced before the vacuum pump (ISP 500C Scroll Meister, Fig. 1). The pressure in the system is monitored and adjusted by a membrane-controlled pressure regulator (see Fig. 1, Equilibar GSD Series Precision Back Pressure Regulator), which allows a range between ~1 mbar and atmospheric pressure. It is well known that CO_2 conversion declines with increasing pressure [3,10,14,15], therefore in this study, we investigate how this changes with quenching by introducing a pressure series from 200 to 900 mbar. Although calculations of the estimated mixture in relation to the explosion regime were completed, there were still safety concerns over injecting CH_4 into the post-plasma afterglow. Therefore, we limited the testing to quasi-atmospheric pressure (900 mbar), as this has been shown to have the same KPIs as atmospheric pressure [18], and so that a larger safety protocol could be implemented for overpressure events that would occur in the instance of an explosion.

The product gas stream is analyzed using an optical oxygen sensor (Pyroscience, GmbH FDO2), and gas chromatography (GC, two-channel, Agilent 990 MicroGC, *SI, S1.5*). Additional details on the diagnostic techniques and performance analysis can be found in *SI, S1.6*.

2.2. Model description

To gain deeper insights into the experimental results, we perform modeling calculations using a 0D chemical kinetics model in the framework of the Chemical Reaction Engineering module of COMSOL Multiphysics [55]. The model solves the 0D mass balance equations for all species in a batch reactor, given by:

$$\frac{d(c_i V)}{dt} = R_i V \tag{E.1}$$

where c_i is the species molar concentration, V denotes the simulation volume and R_i is the species rate expression resulting from chemical reactions. We adopt the GRI-Mech 3.0 reaction mechanism [56] to describe the kinetics of the DRM chemistry, as was also done in *Albrechts* et al. [24].

The initial composition for the simulation is the chemical equilibrium composition of CO_2 at 7000 K, based on our OES measurements, which indicate a peak temperature between ~7000–8000 K (See *SI, S1.3*), representing the hot CO_2 gas core created by the contracted CO_2 plasma. Since our reactor does not utilize heat recovery of the wall losses in the plasma discharge, we assume that 20 % of the energy input is lost through the quartz tube wall, as neglecting heat losses leads to overestimation of the total conversion, and the value of 20 % gave reasonable agreement with experiments. For simplicity, this value is assumed constant across all pressures. Therefore, the specific energy input (SEI, as the amount of power applied to the chemistry in a single pass through the reactor) to the discharge gas (CO_2 primary injection), used to calculate the fraction of CO_2 heated to 7000 K in this work, is multiplied by 0.8:

$$0.8 \bullet SEI = x_p \left(n_{eq} H_{CO_2,eq}(7000\ K) - H_{CO_2}(300\ K) \right) \tag{E.2}$$

In (E.2), x_p represents the molar fraction of CO_2 gas heated to 7000 K, $H_{CO_2,eq}$ indicates the enthalpy of the dissociated CO_2 equilibrium mixture (J/mol), and n_{eq} is a factor that accounts for the increase in the number of particles of the dissociated chemical equilibrium mixture.

At the beginning of the simulation, cold CO_2 (300K) is added via an exponentially decaying source rate, simulating the mixing of the hot CO_2 gas core with the cold surrounding CO_2 flow, as is commonly observed in vortex-stabilized MW plasmas. After a period of 0.67–3.00 ms, depending on the pressure, cold CH_4 (300 K) is introduced to the simulation, according to (E.3). This represents the post-plasma CH_4 injection occurring approximately 5 cm downstream of the waveguide, as reported in the experiments, initiating the DRM chemistry.

$$if\ t > t_{off} : R_m = \frac{n_{CH_4}}{\tau_{mix}} e^{-(t-t_{off})/\tau_{mix}} \quad \text{(E.3)}$$

where t is the simulation time, t_{off} indicates the time interval before the secondary injection of CH_4, R_m represents the mixing rate, i.e. the rate of CH_4 addition to the simulation (mol/s), n_{CH_4} is the total amount of CH_4 added to the system, and τ_{mix} is the characteristic mixing time. We selected a $\tau_{mix} = 10$ ms at the highest pressure of 900 mbar, consistent with the values used in *Albrechts* et al. [24] at atmospheric pressure. The mixing time is scaled proportionally with pressure, as τ_{mix} is inversely proportional to the diffusion constant, which itself is inversely proportional to pressure [24]. The t_{off} is set to 3 ms at the highest pressure of 900 mbar, and is scaled proportionally with pressure, similar to τ_{mix}.

The temperature in the simulation decreases due to mixing with the cold gas (upon secondary injection) and conductive heat losses to the wall [24], eventually quenching the reactive mixture, at which point the simulation is stopped. The model framework used in this study is thoroughly described in *Albrechts* et al. [24]. As explained above, several modifications were implemented, adapting the model to describe our experimental setup, which differs from the configuration used by *Cho* et al. [41], investigated in our previous modeling work [24].

3. Results and discussion

This section presents our findings from both the experimental and modeling investigation of post-plasma reactive quenching with CH_4 in a 2.45 GHz CO_2 MW plasma under two absorbed power (P) conditions, 1000 and 1250 W. Two primary mass flow rates (CO_2) were tested, 10 and 7 standard liters per minute (slm, EU – 20 °C, 1 atm) under varying pressure, and with different secondary injection flow rates (CH_4) to investigate how different ratios of reactive quenching in the afterglow change performance metrics. Our results are organized to address the effects of dual injection on absolute CO_2 conversion and energy cost across various operating conditions, followed by a product distribution analysis, including syngas composition, liquid product formation, and carbon analysis. Our experimental results are supported by our model predictions, which explain the underlying mechanisms.

3.1. Methane as a reactive quenching agent: absolute CO_2 conversion

The data presented in Fig. 3 demonstrates the influence of pressure on CO_2 conversion for a primary flow rate (CO_2) of 10 slm at $P = 1000$ W. We first compare our results with a benchmark measurement of pure CO_2 conversion without secondary injection of CH_4.

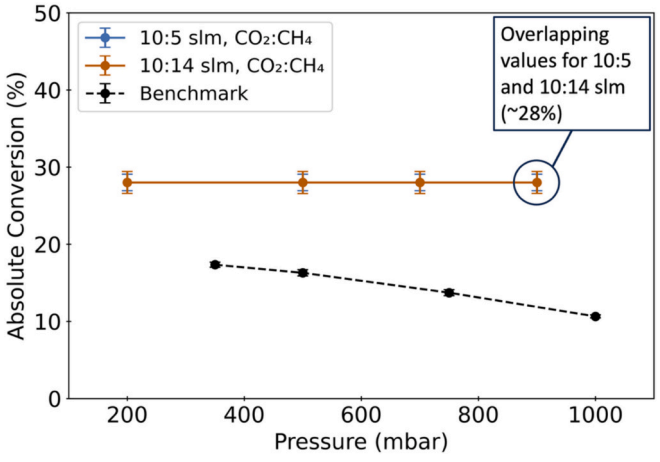

Fig. 3. Absolute CO_2 conversion as a function of pressure for 10:5 slm and 10:14 slm (CO_2:CH_4 ratios) for a primary flow rate (CO_2) of 10 slm and 1000 W, compared to pure CO_2 plasma under the same conditions with no secondary injection (Benchmark). As shown, the data points for the two ratios are identical (~28 %) across all pressures.

In the case of the pure CO_2 plasma without a secondary injection of CH_4 (Fig. 3, *dashed line*), we observe the characteristic pressure dependence of conversion commonly reported in literature [3,15], where, upon increasing pressure, conversion decreases due to enhanced product recombination [12,13,15,57]. Notably, the conversion in the pure CO_2 plasma without post-plasma CH_4 injection is lower across all pressure conditions, ranging from ~18 % at 200 mbar to ~10 % at atmospheric pressure. For both the 10:5 slm and 10:14 slm (CO_2:CH_4) ratios, we observe the same results for conversion (~28 ± 1 %), with no dependence of absolute CO_2 conversion on pressure across the entire range studied (200–900 mbar), and regardless of the secondary injection flow rate of CH_4. This pressure-independent behavior suggests that introducing CH_4 in the post-plasma region effectively mitigates the recombination processes that typically limit CO_2 conversion at higher pressures, even at low flow rates of 5 slm (half the CO_2 flow rate at the inlet). Under these SEI input conditions, we observe that the higher flow rate with the secondary injection of CH_4 (14 slm) does not show additional benefits to absolute CO_2 conversion compared to the lower flow rate (5 slm) of CH_4, both resulting in an almost 3-fold increase in conversion compared to pure CO_2 plasma at atmospheric pressure. This suggests that, beyond a certain threshold, increasing the flow rate of the secondary injection does not promote additional CO_2 conversion, possibly due to saturation of the quenching effect or limitations in the mixing dynamics between the afterglow and the secondary injection.

Fig. 3 clearly illustrates that CH_4 can successfully be used as a quenching gas for CO_2 conversion. The underlying mechanisms are explained in Fig. 4, showing the net rates of different CO_2 conversion reactions as a function of time when CH_4 or Ar are used as a quenching gas, as obtained from our model, for a CO_2:CH_4 (or CO_2:Ar ratio) of 10:14 slm, power of 1250 W, and pressure of 700 mbar. We present this condition as a representative example and note that the relative contributions of the different rates are similar across all conditions. To account for changes in simulation volume over time (due to gas expansion from reactions and temperature increase), we scale the reaction rates by multiplying them by the actual volume and then divide this product by the total number of moles of CO_2 fed into the system throughout the entire simulation, as previously reported in *Albrechts* et al. [24], yielding the rate of CO_2 conversion expressed in s^{-1}.

The dominant reactions governing CO_2 conversion in our model are:

$$CO_2 + M \leftrightarrows CO + O + M \quad \text{(R.1)}$$

$$CO_2 + O \leftrightarrows CO + O_2 \quad \text{(R.2)}$$

$$CO_2 + H \leftrightarrows CO + OH \quad \text{(R.3)}$$

where (R.1) shows the thermal dissociation reaction (which occurs upon collision with a third body, denoted as M), (R.2) represents dissociation upon collision with O atoms, and (R.3) is H-mediated conversion. Indeed, we can assume the chemistry is thermal, both inside the plasma (due to the high temperatures of 7000 K) and in the afterglow (where electrons and ions are no longer present). The rate coefficients are defined by the GRI-Mech 3.0 reaction mechanism [56], where the reverse rates are calculated according to the principle of detailed balance.

As shown in Fig. 4.A, at the start of the simulation, CO_2 is primarily converted through thermal dissociation (R.1) due to the very high temperatures ($T > 5000$ K). As the temperature decreases due to the addition of cold CO_2, the contribution of thermal dissociation decreases, and the reaction of CO_2 with O (R.2), which has a significantly lower energy barrier, becomes the dominant CO_2 conversion pathway. Around $t = 0.83$ ms, the rate of R.1 becomes negative, indicating that the reverse reaction becomes dominant, as there is insufficient energy for efficient thermal dissociation of CO_2, resulting in net creation of CO_2 by this reaction.

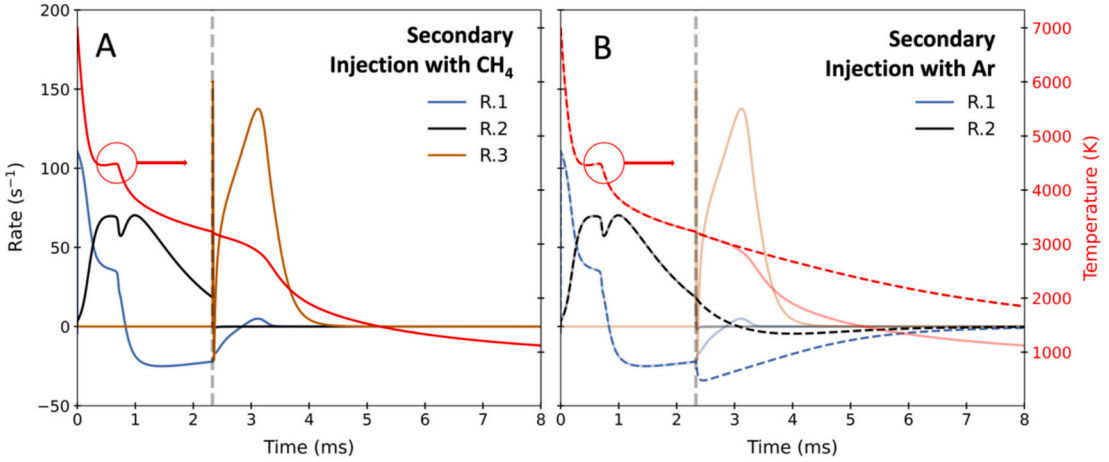

Fig. 4. Calculated net rates (s^{-1}) of CO_2 conversion as function of time (ms), for secondary injection quenching with CH_4 (4.A, solid lines) and Ar (4.B, dashed lines), at a pressure of 700 mbar, a power of 1250 W and CO_2:CH_4 (or CO_2:Ar) ratio of 10:14 slm. The temperature (K, red) is plotted on the right y-axis. The vertical dashed grey line indicates the instance of CH_4 (or Ar) injection ($t = 2.33$ ms). The reference rates for CH_4 quenching have been shaded in Fig. 4.B for easy reference. The graph demonstrates that the temperature decreases more rapidly when CH_4 is used as a quenching gas, due to its higher heat capacity compared to Ar.

Initially, the temperature is sufficiently high for the O atoms to convert more CO_2 via (R.2); however, as the temperature decreases, the destruction of CO via the reverse reaction of (R.1) (which has a significantly lower energy barrier) becomes more prominent compared to the forward rate of (R.2), leading to net CO_2 production when the temperature drops below approximately 3000 K, as indicated by the model. This is where cold CH_4 is introduced into the simulation, i.e., at $t = 2.33$ ms, representing the post-plasma injection of CH_4, as indicated by the sudden presence of CO_2 conversion by H atoms (R.3). One of the reasons for using CH_4 as a quenching gas for CO_2 conversion is to remove O atoms through CH_4 oxidation, thereby preventing it from reacting with CO to form CO_2 and enhancing the net CO_2 conversion. This is evident from Fig. 4.A, which shows that the net rate of CO destruction via (R.1) rapidly drops to zero after CH_4 injection, preserving more of the CO produced in the hot CO_2 mixture. The results demonstrate that CH_4 injection provides enhanced performance through two complementary chemical pathways: (1) effective suppression of CO recombination reactions, and (2) additional CO_2 conversion via the reverse water-gas shift (RWGS) reaction.

To further elucidate the specific advantages of using CH_4 as a reactive quenching agent, we conducted additional modeling calculations comparing CH_4 injection with inert Ar quenching under identical conditions to the 10:14 slm CO_2:CH_4 ratio at 1250 W and 700 mbar, as shown in Fig. 4.B. This comparison reveals two distinct mechanisms by which CH_4 enhances CO_2 conversion compared to thermal quenching. Fig. 4.A presents the calculated net rates of CO_2 conversion reactions for both CH_4 (transparent solid lines) and Ar (dashed lines) quenching.

When cold Ar gas is injected as a quenching agent, significant CO recombination occurs through the reverse of (R.1). This is evidenced by the pronounced negative peak at $t = 2.33$ ms, corresponding to the moment of injection, which destroys ~30 % of the CO present upon injection of Ar. In contrast, when CH_4 is used, CO destruction due to recombination with O atoms is negligible (< 1 %), owing to the efficient scavenging of O atoms through CH_4 oxidation. We observe that CH_4 effectively scavenges these O atoms through oxidation reactions (e.g., $CH_4 + O \rightarrow CH_3 + OH$), before they can participate in recombination with CO, resulting in <1 % destruction of CO upon CH_4 injection. In addition to suppressing CO recombination, Fig. 4.A highlights a substantial additional CO_2 conversion attributed to reactions with H atoms, linked to the RWGS reaction. This reaction accounts for approximately 33 % of total CO production, effectively generating an additional 50 % of the CO present at the instance of quenching. These combined effects lead to a notably higher CO_2 conversion of 36.1 % when CH_4 is used as a quenching agent, compared to only 15.8 % when cold Ar is injected post-plasma.

The calculation from Fig. 4.B demonstrates that the temperature decreases more rapidly when CH_4 is used as a quenching gas, due to its higher heat capacity compared to Ar; however, it is important to note that the enhanced cooling effect of CH_4 as a quenching agent contributes minimally to the mitigation of CO recombination. Although CH_4 provides a higher cooling rate compared to Ar, the temperature profiles remain similar during the critical timeframe of $t < 3.3$ ms due to the compensatory exothermic oxidation reactions. During this timescale, all O atoms undergo recombination, rendering CO recombination (R.1) insignificant when temperature divergence begins. As a result, we conclude that the stronger cooling effect of CH_4 does not significantly influence CO_2 conversion. This highlights the importance of not only fast cooling, but also quickly removing O atoms in the afterglow region.

The model predictions convincingly demonstrate that CH_4 addition removes the O atoms, thereby preventing them from reacting with CO to form CO_2 again. In addition, the CH_4 addition provides H atoms upon dissociation/oxidation, which also contributes to CO_2 dissociation. Both mechanisms, predicted by the model, explain the enhanced CO_2 conversion upon post-plasma CH_4 injection. In Fig. 5, we investigate the overall changes to the absolute conversion of CO_2 and CH_4 as a function of plasma power, for a primary flow rate (CO_2) of 10 slm.

The data is organized into two graphs by the secondary injection flow rate of CH_4 (Fig. 5.A 10:5 slm, CO_2:CH_4 and Fig. 5.B 10:14 slm, CO_2:CH_4), for two power conditions ($P = 1000$ W, solid and 1250 W, striped). The data at $p = 500$ mbar, 1250 W for 10:5 slm, CO_2:CH_4 is unavailable. A clear trend emerges when comparing the effect of the secondary injection CO_2:CH_4: increasing the flow rate consistently decreases its absolute conversion, observed both in the experiment and modeling results. This is likely a result of the lower effective *SEI* (i.e., total *SEI* distributed between both reactant gases). Note that the CO_2 conversion without post-plasma CH_4 injection is between ~18–10 % (respective to increasing pressure, see also Fig. 3) across all conditions, demonstrating a clear enhancement from reactive quenching, which is most pronounced at higher power, and thus, higher *SEI*.

For example, at $P = 1250$ W, $p = 900$ mbar with a primary flow rate of 10 slm CO_2, we observe the highest absolute CH_4 conversion (~34 ± 4 %) when using a relatively low secondary injection flow rate (10:5 slm, CO_2:CH_4, Fig. 5.A), with a clear increase compared to $P = 1000$ W, p = 900 mbar conditions (~24 ± 4 %). As mentioned, we also observe that the absolute conversion of CH_4 drops significantly when the secondary injection increases to 14 slm. For exampla, at $P = 1250$ W, $p = 900$ mbar,

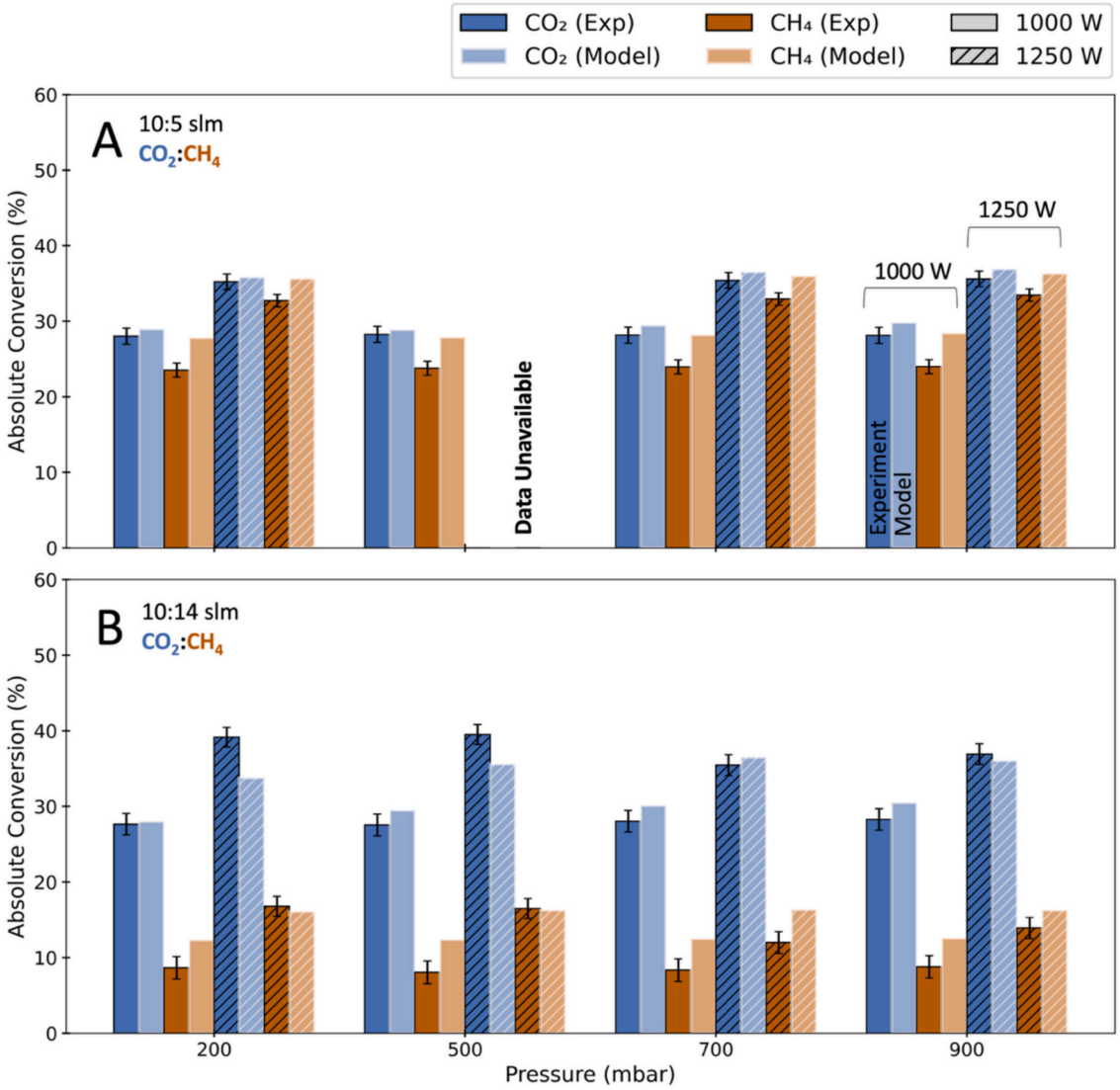

Fig. 5. Comparison of absolute CO_2 and CH_4 conversion for a primary flow rate of 10 slm of CO_2 with different post-plasma flow rate injections of CH_4 A) 10:5 slm CO_2:CH_4 (P = 1000 W, solid and 1250 W, striped), and B) 10:14 slm CO_2:CH_4 (P = 1000 W, solid and 1250 W, striped). The modeling results are presented with overlayed white stripes directly next to the experimental data. In cases where data collection was not possible due to technical constraints, the corresponding data points are marked as 'Data Unavailable.'

the absolute conversion of CH_4 is ~14 ± 2 % (10:14 slm, CO_2:CH_4 ratio, Fig. 5.B). We note that increased power directly enhances conversion, which can be observed in Table 1, where we show the absolute increase of conversion between P = 1250 W and 1000 W for the conditions presented in Fig. 5.

Importantly, we note that the model correctly captures the absolute CO_2 conversion under the conditions presented in Fig. 5.A and B, but is not able to capture the slight increase in CO_2 conversion upon decreasing pressure in Fig. 5.B, P = 1250 W, p = 200 mbar, see also Table 1. However, overall, there is reasonable agreement between the absolute conversion of both CO_2 and CH_4 calculated by the model and the experimental data. Furthermore, the trends presented in Fig. 5 suggest that there may be an optimal ratio between the injection of the primary flow rate and the secondary flow rate that maximizes the conversion of both feed gases, for example, when the secondary injection flow rate is smaller than the primary injection flow rate. The reader should note that when the secondary flow rate is lower than the primary flow rate, pressure gradients can develop that may destabilize the plasma, potentially extinguishing the discharge. Therefore, the stability of this dual-injection configuration depends critically on the positioning of the secondary injection. In our experimental setup, we mitigated this by placing the secondary injection approximately 5 cm downstream from the waveguide, providing sufficient distance to maintain stable plasma operation across all tested conditions, however, moving the secondary injection closer to the plasma may also serve to enhance conversion of the secondary reactant. We will now examine the results

Table 1
Absolute increase (%) of conversion between 1000 W and 1250 W for the conditions presented in Fig. 5 (10 slm primary inlet of CO_2).

Ratio (CO2: CH4, slm)	Pressure (mbar)	CO_2 Conversion Absolute Increase (%)	CH_4 Conversion Absolute Increase (%)
10:5	200	7	9
10:5	500	N/A	N/A
10:5	700	7	9
10:5	900	7	9
10:14	200	12	8
10:14	500	12	8
10:14	700	7	4
10:14	900	9	5

for increased *SEI*, with a primary flow rate of 7 slm, shown in Fig. 6.

Higher SEI to the discharge gas presented in Fig. 6 provides a comparison of absolute conversion performance across four experimental configurations, where the data is organized in the same manner as described in Fig. 5. The results show deviations from some of the findings with a primary flow rate of 10 slm (Fig. 5).

First, in Fig. 6 we note that higher *SEI* to the discharge gas consistently shows better absolute conversions compared to the conditions presented in Fig. 5 across all flow configurations. For example, the best overall performance shown in Fig. 6.A is noted for $P = 1250$ W (7:7 slm, CO_2:CH_4), where the absolute conversions of CO_2 and CH_4 reach 55 ± 1 % and 37 ± 1 %, respectively, at $p = 500$ mbar. Notably, under these conditions, the pressure-independence of conversion deviates slightly, with enhanced absolute conversion of CO_2 and CH_4 with decreasing pressure from 900 mbar, which can also be observed in the absolute increase shown in Table 2. We will examine these findings in greater detail in *Section 3.2* below.

It is clear from these results that a higher *SEI* to the discharge gas facilitates an increase in CO_2 dissociation within the reactive volume and will subsequently increase the temperature of the afterglow region, in turn allowing more energy exchange and greater conversion of both the primary reactant (CO_2) and the reactive quenching gas (CH_4).

As discussed in Section 2, the secondary injection housing was designed to monitor the afterglow region for carbon formation in real time, with an additional quartz tube placed downstream of the secondary injection. Although a qualitative observation is all we can make regarding carbon formation, we feel it is worth noting that during the experiments, no carbon formation was visible below 700 mbar. Upon transition between 700 and 900 mbar, characteristic irradiance of carbon particles appeared in the afterglow region, noted as an orange 'flame-like' plume, which became more pronounced as the pressure increased to 900 mbar. This plume was the largest at higher power

Table 2
Absolute increase (%) of conversion between 1000 W and 1250 W for the conditions presented in Fig. 6.

Ratio (CO2:CH4, slm)	Pressure (mbar)	CO_2 conversion absolute Increase (%)	CH_4 conversion absolute increase (%)
7:7	200	N/A	N/A
7:7	500	15	17
7:7	700	13	10
7:7	900	10	7
7:14	200	N/A	N/A
7:14	500	11	4
7:14	700	12	5
7:14	900	12	4

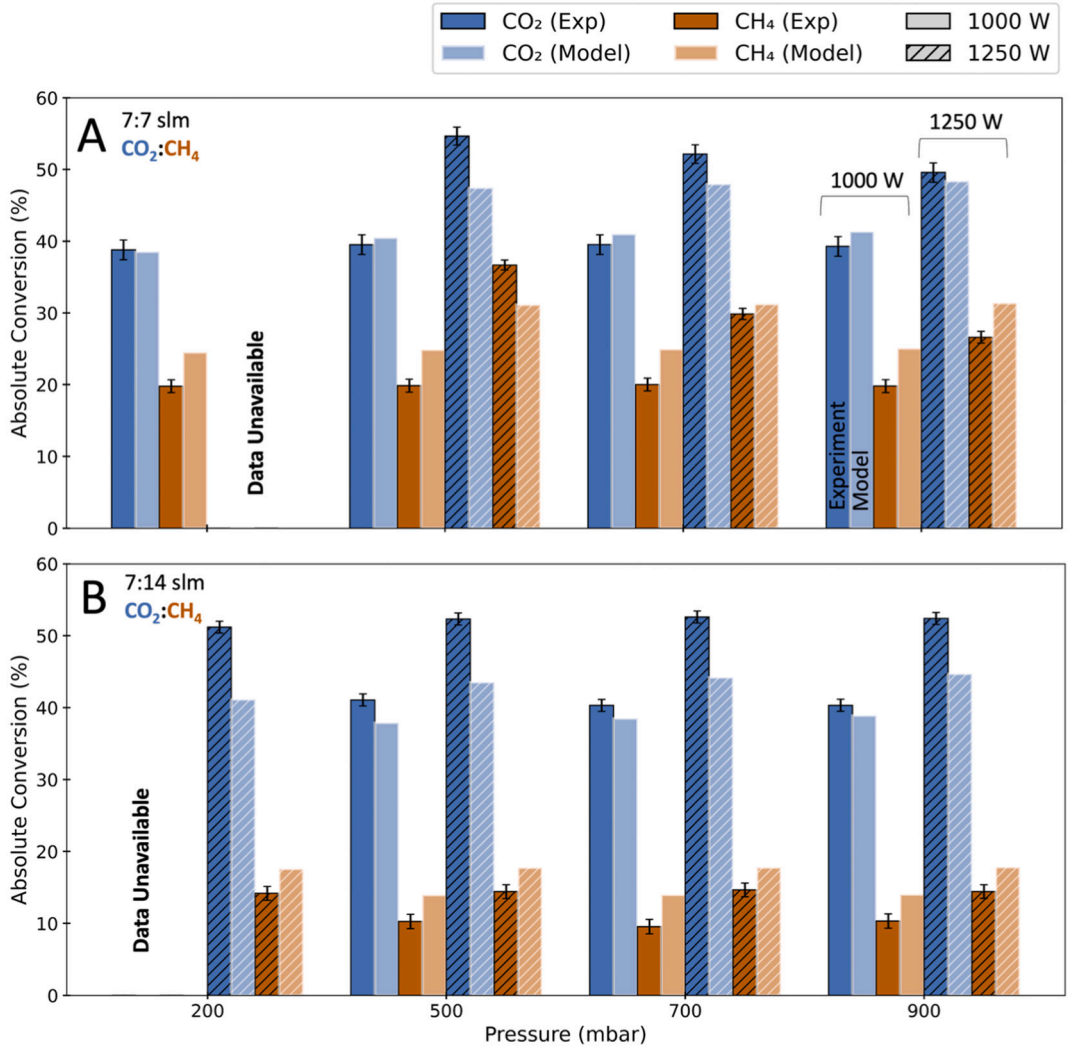

Fig. 6. Comparison of absolute CO_2 and CH_4 conversion for a primary flow rate of 7 slm of CO_2 with different post-plasma flow rate injections of CH_4 (see text), for two power conditions (P = 1000 W and 1250 W), A) 7:7 slm CO_2:CH_4 and B) 7:14 CO_2:CH_4. In cases where data collection was not possible due to technical constraints, the corresponding data points are marked as 'Data Unavailable.'

conditions (P = 1250 W); however, overall, the formation of carbon particulates was still found to be minimal, only appearing downstream as a 'light' deposit along the walls. Most importantly, by injecting CH_4 into the post-plasma region, we observe that the carbon formation occurs downstream of the discharge; therefore, whatever carbon is formed does not interact with the MW field and thus allows for higher CH_4:CO_2 feed gas ratios, resulting in higher syngas ratios (see Section 3.2).

In summary, we examined how injecting CH_4 as a reactive quenching agent into the post-plasma region affects the absolute CO_2 conversion under various operating conditions. We saw in Fig. 3 that when CH_4 is used as a reactive quenching agent, the CO_2 conversion remains constant (~28 %) across all pressures (p = 200–900 mbar), regardless of the CO_2:CH_4 ratio. This contrasts with pure CO_2 plasma, where the final conversion decreases with increasing pressure due to recombination; therefore, we attribute the pressure-independent conversion to effective mitigation of the recombination processes that typically limit CO_2 conversion at higher pressures through reactive quenching with CH_4, confirmed by modeling. Chemical kinetics modeling shows that CH_4 injection enhances the CO_2 conversion through two mechanisms: (1) removing O atoms that would otherwise cause CO to recombine back to CO_2, and (2) providing H atoms through CH_4 dissociation, which further promote CO_2 conversion. Higher power and higher *SEI* show improved absolute CO_2 conversion, with the best performance (~55 %) achieved at p = 500 mbar with a 7:7 slm, CO_2:CH_4 ratio.

Having established that injecting CH_4 as a reactive quenching agent into the high-temperature afterglow region of a CO_2 plasma enhances CO production, we will now examine how this approach performs as a method for DRM. By analyzing key performance metrics such as syngas ratio and product selectivity, we can fully understand both the potential and limitations of this dual injection approach compared to the conventional (admixing) DRM processes.

3.2. A dry reforming of methane perspective: syngas ratio and product selectivity analysis

As discussed in the introduction, the difficulty in controlling the produced syngas ratio (i.e., H_2:CO) presents a critical limitation when admixing CO_2 and CH_4 in plasma-based DRM. Therefore, we explore the effect of the ratio of primary and secondary injection on the syngas fraction, shown in Fig. 7 below, for p = 900 mbar, where we were able to investigate up to 1:2 ratios (7:14 slm) of CO_2 and CH_4. All syngas (H_2:CO) ratios can be found in *SI, Section S.3.1*.

Fig. 7 presents an analysis of both the Energy Cost (EC, in kJ/mol and eV/molecule, primary y-axis, calculated accounting for both reactants, CO_2 and CH_4) and the syngas ratio (H_2:CO, secondary y-axis). Further details on the calculations can be found in *SI, Section S.1.6*. The data reveals a direct correlation between the secondary CH_4 flow rate and the H_2:CO ratios, confirming that increasing the post-plasma CH_4 injection does increase the syngas ratio; however, the maximum syngas ratio observed at p = 900 mbar was only 0.37 ± 0.02, at the highest CH_4

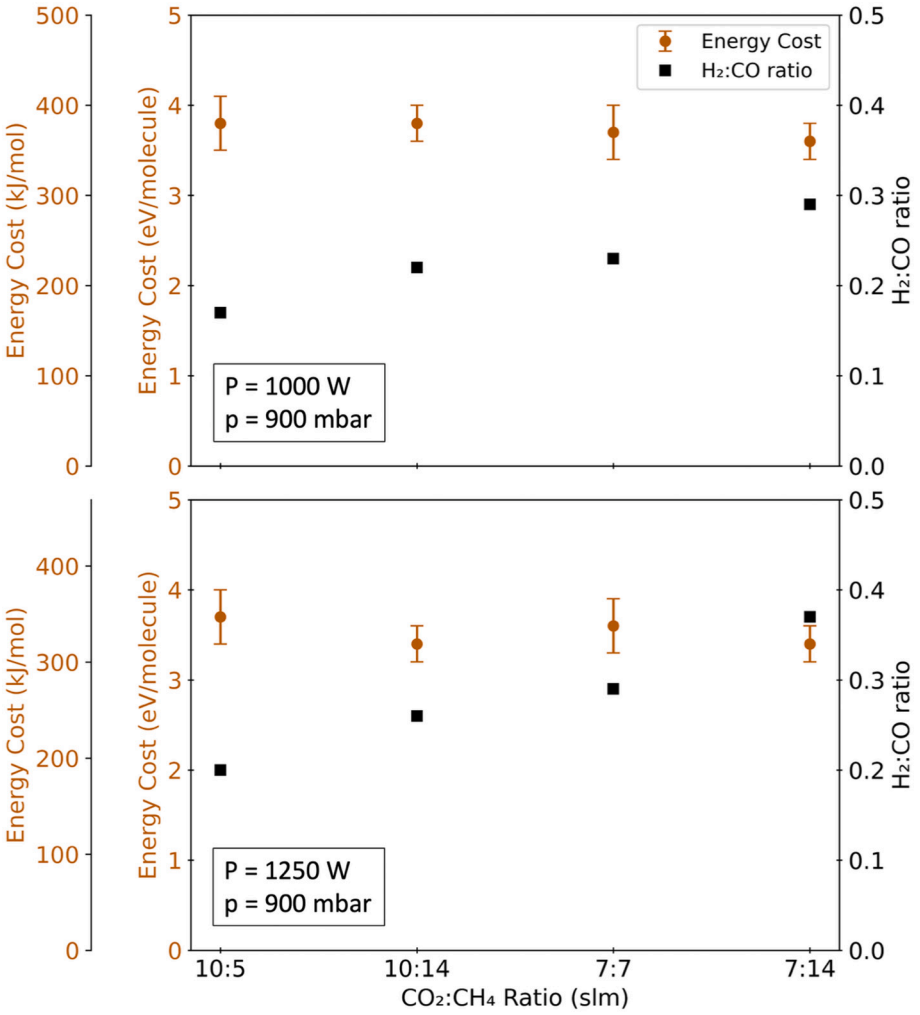

Fig. 7. Energy cost (kJ/mol and eV/molecule) on the primary y-axis, and H_2:CO (syngas) ratio on the secondary y-axis as a function of the CO_2:CH_4 ratio, at p = 900 mbar. A primary flow rate of 10 slm is represented in the left most markers, and 7 slm in the right most markers, for A) 1000 W and B) 1250 W.

fraction (1:2 ratio, 7:14 slm) and $P = 1250$ W.

Although the *SEI* varies slightly between our conditions (i.e., *SEI* = 132 kJ/mol at a 7:7 slm, CO_2:CH_4 ratio) and those reported by *Kelly* et al. for conventional DRM (*SEI* = ~144 kJ/mol) [42], our EC is higher at p = 900 mbar, $P = 1000$ W (346 ± 17 kJ/mol) compared to values $\lesssim$ 269 kJ/mol at the same power in *Kelly* et al. [42]. However, under the same conditions (*SEI* = 132 kJ/mol, 7:7 slm, CO_2:CH_4) at lower pressure (p = 500 mbar), we obtained an EC as low as 289 ± 15 kJ/mol, with a syngas ratio of 0.38 ± 0.02, see *SI, Section S.3.1*. This is the same condition discussed in Section 3.1 where we observed an absolute CO_2 conversion of ~55 % (see Fig. 6.B). Importantly, the highest H_2:CO ratio for our quasi-atmospheric results, i.e., 0.37 ± 0.02 (for 7:14 slm CO_2:CH_4, *SEI* = 89 ± 4 kJ/mol; EC = 325 ± 16 kJ/mol), is less than half of the best reported value for conventional (admixing) DRM in the MW plasma, reported by *Kelly* et al. [42], and the dual injection with the extended reforming chamber reported in *Cho* et al. [41] (1:1 CO_2:CH_4 ratio, syngas ratio of ~1, EC = 245 kJ/mol). This is likely due to a limitation of operational conditions (lower *SEI* achievable in our reactor), and the quenching effect limiting the conversion of the quenching reactant, CH_4, in the afterglow.

Fig. 8 presents a comprehensive analysis of product selectivity of gaseous products as well as unknown fractions at $P = 1250$ W across different pressure conditions and flow configurations. Calculations were made based on GC measurements of gas phase species. Tables with the values can be references in *SI, S.3.1, Tables S.2 – S.33*. The data is organized by the primary flow rate of CO_2 (10 slm in Fig. 8.A and B; 7 slm in Fig. 8C and D) and the secondary flow rate of CH_4 (lower in Fig. 8A and C; higher in Fig. 8B and D).

All conditions show a high selectivity toward CO formation, particularly prominent in the 10:5 slm and 7:14 slm, CO_2:CH_4 ratios. The relatively low syngas ratio observed in our experiments (as previously shown in Fig. 7) can be directly attributed to suboptimal H_2 selectivity across these conditions, which prevents achieving higher syngas ratios under the conditions presented in this work (i.e., *SEI* to the discharge gas). The 7:14 slm, CO_2:CH_4 ratio demonstrates the strongest selectivity toward H_2, corresponding with an absolute H_2 outflow rate of ~1.5 slm (vs. 14 slm of CH_4 input flow rate). To gain deeper insight into the low CH_4 conversion and H_2 selectivity, we employed the 0D chemical kinetics model to understand the dominate reaction mechanisms.

As shown in Fig. 9, the model aligns reasonably well with the experimental selectivities across most conditions; however, note that the model tends to considerably overestimate the H_2 selectivity, which is especially prominent at higher CH_4 fractions. This is linked to the significant fraction of unknown C (e.g., hydrocarbons, aromatics, oxygenates) seen in the experiments, which is not captured by the model. Similarly, the model does not accurately capture the selectivity toward the C_xH_y hydrocarbons, particularly at low pressure (p < 500 mbar); although the reader should note that the total selectivity of C_xH_y species found in the experiments was low across all conditions (< ~6 % for C-based, and < ~10 % for H-based selectivity), and due to their low concentrations, exhibit a high uncertainty (see *SI, Section S.3.1*). As a result, it is difficult to highlight their individual contributions to selectivity.

As an example, for a ratio of 7:7 slm, we find the C-based selectivity of C_2H_x to be ~1.8 % at $p = 900$ mbar with an even distribution among species, whereas the model shows ~4.8 %, with the greatest contribution from C_2H_2 (~4.4 %). This discrepancy suggests that the reactive pathways leading to C_xH_y hydrocarbons and species constituting the unknown C fraction are not sufficiently represented by the global model, as they would require accurate resolution of the temperature gradients and species transport within the reactor, but this is outside the scope of a 0D model which cannot describe these complex dynamics. Nevertheless,

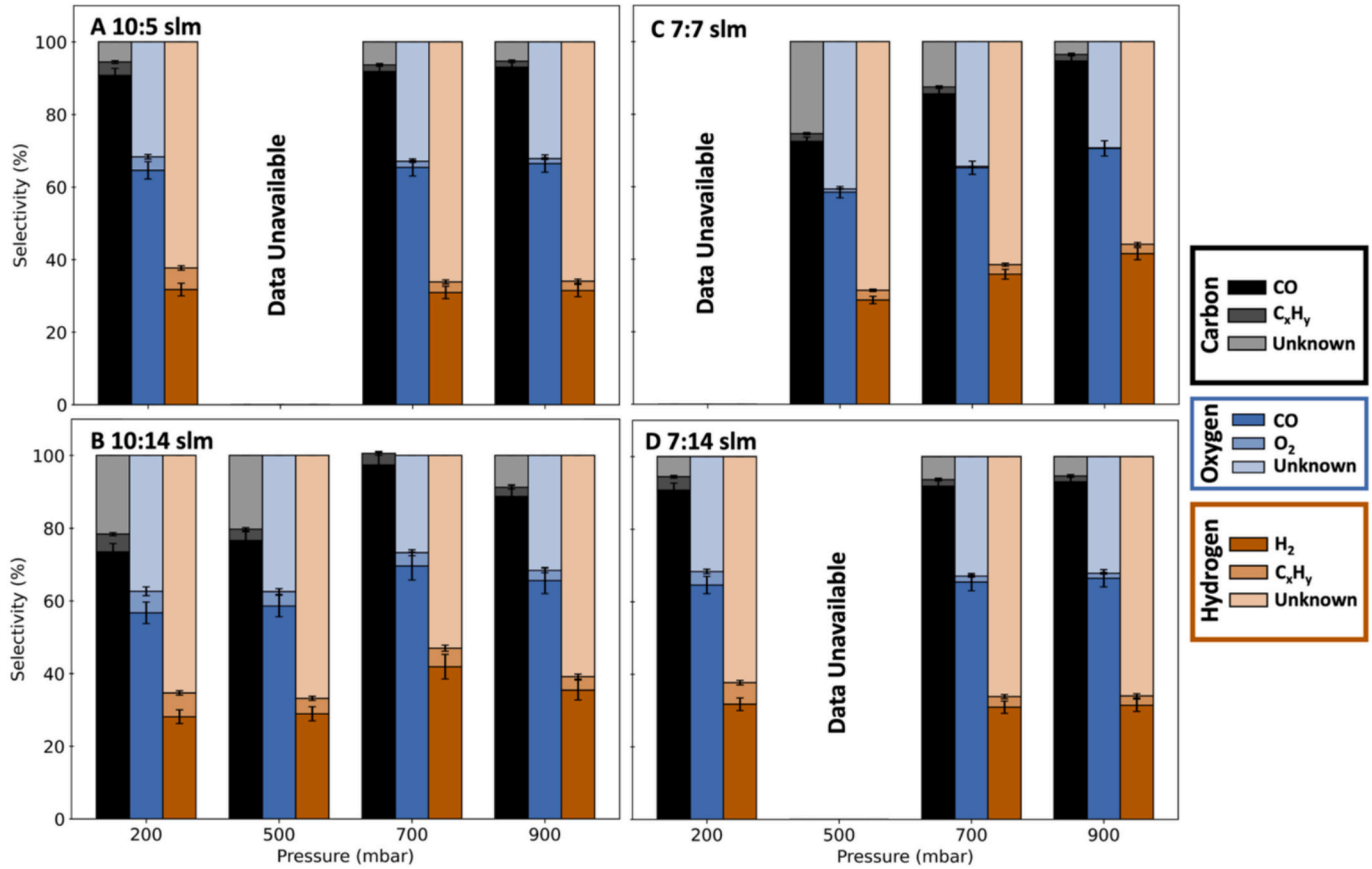

Fig. 8. Selectivity comparison for P = 1250 W for a primary CO_2 flow rate of 10 slm (A and B) and 7 slm (C and D), with different post-plasma injection flow rates of CH_4 (see text). In cases where data collection was not possible due to technical constraints, the corresponding data points are marked as 'Data Unavailable.'

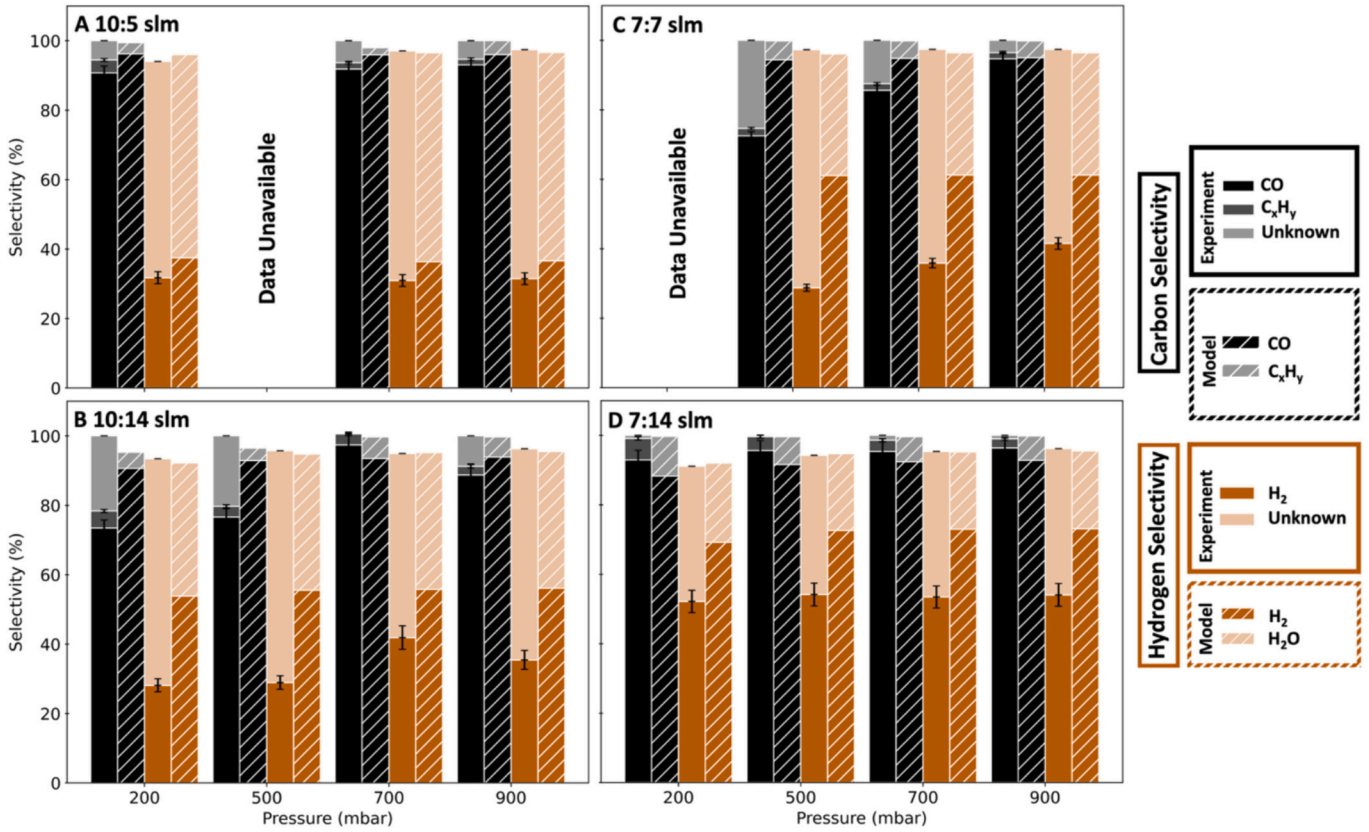

Fig. 9. Comparison between experimental and calculated selectivities at P = 1250 W for a primary CO_2 flow rate of 10 slm (A and B) and 7 slm (C and D), with different post-plasma injection flow rates of CH_4. Only the selectivities toward hydrogen and carbon are plotted, because the O-based selectivities do not provide additional information. In cases where data collection was not possible due to technical constraints, the corresponding data points are marked as 'Data Unavailable.'

the overall agreement is quite reasonable, especially for the main DRM metrics, i.e., CO_2 and CH_4 conversion and CO and H_2 selectivity. Multidimensional kinetic simulations employing the GRIMECH 3.0 mechanism could potentially improve the selectivity toward C_xH_y gaseous species by resolving kinetic pathways that require accurate modeling of temperature gradients and species transport. However, given that the reaction mechanism does not account for solid carbon formation, the overestimation of H_2 selectivity would likely persist. Thus, to adequately model solid carbon formation, the GRIMECH set would need to be complemented with additional mechanisms, such as the polycyclic aromatic hydrocarbon (PAH) mechanism, which is highly complex and comprises an extensive number of species, rendering it impractical for multidimensional modeling. While this would be an interesting avenue for future research, it falls outside the scope of the present study.

A high percentage of unknown O-based and H-based selectivity is reported across all conditions (Fig. 8). Particularly, for ratios of 10:5 and 7:14 slm (CO_2:CH_4), we observe a pattern of missing H and O atoms in proportions close to 2:1, suggesting substantial H_2O formation with minimal unaccounted carbon. The model provides important insights into the reaction pathways responsible for this H_2O formation, showing that when CH_4 is injected into the high-temperature post-plasma region as a reactive quenching agent, it scavenges O atoms, predominantly through the reaction $CH_4 + O \rightarrow CH_3 + OH$, and subsequently CH_3 will further consume O atoms via reactions $CH_3 + O \rightarrow H + CH_2O$ and $CH_3 + O \rightarrow H + H_2 + CO$. As CH_4 is rapidly oxidized to CO in the complex reaction pathways stated above, H atoms are released that subsequently react with CO_2 via the reaction $CO_2 + H \rightarrow CO + OH$. This represents part of the RWGS reaction mechanism, where the equilibrium between CO_2, H_2, CO, and H_2O is governed by temperature. Our model reveals that H_2O formation peaks at a concentration of approximately 20 % when gas temperatures reach ~2800 K, following the water-gas shift equilibrium. However, as the temperature rapidly decreases below 2000 K, the reaction kinetics slow down considerably, effectively "freezing" the H_2O concentration around 6 %, despite the equilibrium favoring its decomposition at lower temperatures. This kinetic limitation prevents the formation of H_2, resulting in the low H_2 selectivity observed in our experiments, as explained in detail in *SI, S.2.1.* Consequently, although the post-plasma CH_4 injection enhances CO_2 conversion through a reaction with H atoms (as shown in the high absolute conversion compared to pure CO_2 conversion in Fig. 3), it simultaneously promotes substantial H_2O formation, explaining the significant fraction of unknown H and O atoms in the selectivity, as shown in Fig. 8.

This trade-off between improved CO_2 conversion and H_2O formation represents a key limitation in achieving higher syngas ratios in our current reactor configuration at this relatively low *SEI*, which confirms the modeling results published by *Albrechts* et al. [24]. Importantly, our model reveals that higher *SEI* and CH_4 ratios (240 kJ/mol or ~ 12 eV/molecule, 1:4 ratio of CO_2:CH_4) may result in a higher conversion of both CO_2 and CH_4, yielding a significantly better syngas ratio (~2), as discussed in detail in *SI, S.2.2.* However, we note that this *SEI* is much higher than typical inputs found in literature, with the highest reported values found to range between 7 and 8 eV/molecule [15,58]. Importantly, it is expected that solid carbon formation will increase with higher CH_4 fractions and elevated *SEI* values, as this is inherent to the stoichiometry of the DRM process under CH_4-rich conditions, where insufficient oxygen is available to oxidize all CH_4, resulting in the formation of hydrocarbons that either remain in the gas phase or nucleate into solid carbon, enabling high syngas ratios. In the model calculations, excess CH_4 is converted exclusively into gaseous C_xH_y hydrocarbons, without contributing to solid carbon formation. Thus, the impact on CO and H_2 yields will ultimately depend on the extent of solid carbon

formation. Therefore, experimental validation of higher *SEI* conditions would be valuable to assess whether the promising syngas yields and ratios predicted by the model, which excludes solid carbon formation, can be realized in practice.

Notably, as reported in Figs. 8 and 9, selectivity patterns remain largely independent of pressure. An exception to this is observed in the unknown fraction of species (obtained from carbon, hydrogen, and oxygen balances). The observed formation of solid carbon was found to be minimal across all conditions and not observed at $p < 700$ mbar, which is in line with the selectivity data reported in Fig. 8. For example, the unknown C fraction in Fig. 8.B at $p = 900$ mbar is likely attributed to solid carbon formation, which correlates with our observations of a 'flame-like' plume in the post-plasma region under these conditions. Furthermore, a minimal amount of solid carbon was found in the cyclone separator. Although the model points to substantial H_2O formation, the unknown values for 10:14 and 7:7 slm, CO_2:CH_4 at $p \leq 500$ mbar, as shown in Fig. 8.B and C, tell a slightly different story, where we find a large fraction of unknown C atoms (between ~10–25 %). Therefore, the unknown fraction of C under these conditions suggests the formation of products beyond the measured gaseous species and likely points toward the formation of liquid products that will be examined below.

Quantification of liquid products helps us to understand these trends further. To limit the number of samples, we collected a single liquid sample for each CO_2:CH_4 ratio investigated, meaning for both power conditions and all pressure sets, which was analyzed using the methods outlined in *SI, S.1.1,* to determine the composition. In each of the samples collected, the liquid was yellow, with the 7:7 slm, CO_2:CH_4 mixture being the darkest. The samples exhibited '*a strong, sweet, petrol-like odor*', typically associated with hazardous chemicals. We also note that all the post-plasma bellows were stained yellow. The analysis revealed that although the liquid was predominantly water (as the model predicts, which correlates with high unknown O and H selectivities presented in Fig. 8A and D, and at higher pressure in Fig. 8B and C), three other main compounds were identified: formaldehyde, acetic acid, and formic acid. Each of these species are present at all ratios of CO_2:CH_4; however, the concentration varies according to the ratio, as shown in Fig. 10.

As shown in Fig. 10, formaldehyde, acetic acid, and formic acid are detected, with formaldehyde as the highest concentration at ~3200 ± 160 ppm at 7:7 slm CO_2:CH_4 ratio. The reader should keep in mind that although the samples were taken per ratio, based on the selectivity data, a correlation between the oxygenates detected and the unknown species ratios in the 7:7 slm and 10:14 slm CO_2:CH_4 samples suggests that these molecules of interest are likely formed in greatest concentration at $p \leq 500$ mbar at $P = 1250$ W (Fig. 8.B and C). The extreme temperatures ($T >> 1000$ K) found in the reactive volume and afterglow generate radicals that can produce a variety of compounds from CH_4 and CO_2. Furthermore, we link the dependency between the model and experimental selectivity (Fig. 9) to the significant fraction of unknown C, from for e.g., hydrocarbons, aromatics, oxygenates), which is not captured by the model since GRIMECH 3.0 is exclusively a gas-phase reaction mechanism, it does not include reactive pathways leading to solid carbon formation. Noting the oxygenates measured in the water fraction are too dilute to explain the substantial unidentified carbon fraction, we believe that the majority of the unknown carbon species consists of solid carbon carried away as nanoparticles at lower pressure, where coagulation/agglomeration may not occur, and therefore, the carbon would not be captured by the cyclone separator. Consequently, the model overpredicts the gaseous carbon species, particularly CO and C_xH_y compounds. In reality, the gaseous CO that would ultimately contribute to soot formation would consume H atoms while simultaneously generating H_2O due to stoichiometric constraints, both factors contributing to the observed overestimation of H_2 selectivity by the model.

However, we conjecture that CH_4 fragmentation and CO_2 dissociation (CO + O) lead to the formation of these oxygenates, and especially CO + H_2 can form formaldehyde [59], which could also explain the reduction in CO and H_2 selectivity under these conditions (Fig. 8.B and C), although a reaction between $\cdot CH_3$ and O is also possible [60]. As shown in Fig. 11, we investigated the total carbon count and analyzed the spectrum of the 7:7 slm, CO_2:CH_4 sample using UV–Vis, as the presence of these oxygenates did not fully explain the yellow hue of the liquid collected.

Fig. 11.A presents the theoretical total carbon count calculated from the concentration in the samples detected using high performance liquid chromatography (HPLC) and the measured total organic carbon (TOC) in the sample. Comparison of both allows us to assess the completeness of compound identification. The difference is small, indicating that much of the carbon-containing species have been accounted for in the

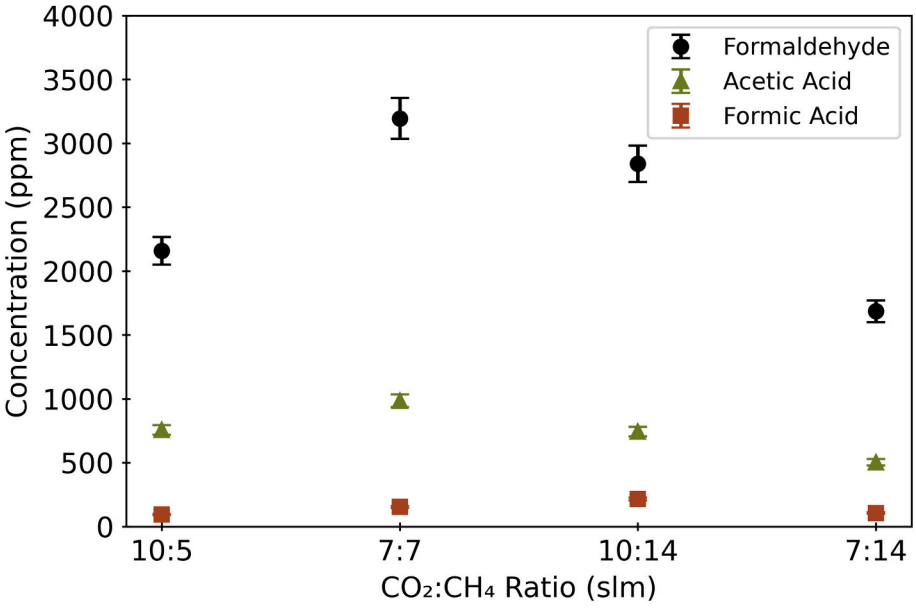

Fig. 10. Concentration (ppm) of the three main components found in each data set (ratio CO_2:CH_4). The highest concentration of formaldehyde, the second highest concentration of a single constituent other than water, was found in the 7:7 and 10:14 slm CO_2:CH_4 ratios, where we observed the largest unknown quantities of C, O, and H species.

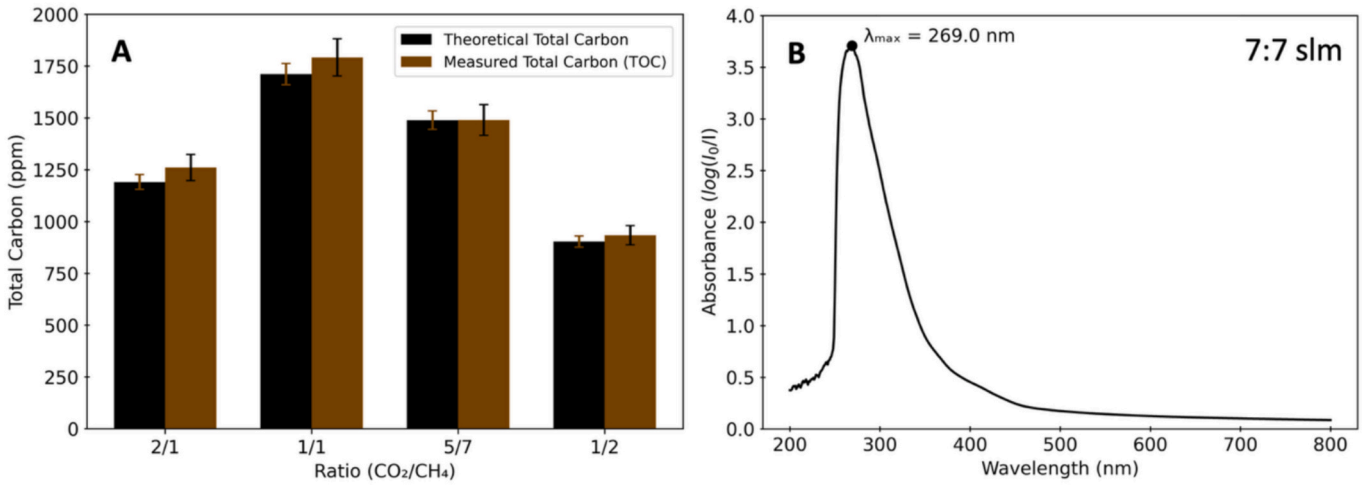

Fig. 11. A: Theoretical total carbon count of the samples, as measured by HPLC (black), and measured by TOC analysis. B: UV–Vis spectrum from the 7:7 slm, CO_2:CH_4 sample with a sharp peak (λ_{max}) found at 269 nm, indicative of a $\pi \rightarrow \pi^*$ electronic transition in a conjugated system.

analysis. The UV–Vis analysis (Fig. 11.B) reveals λ_{max} at 269 nm, suggesting a $\pi \rightarrow \pi^*$ electronic transition from a conjugated system. In general, simple carbonyls (like formaldehyde and acetic acid) absorb only in the deep – mid UV and produce peaks between ~190–250 nm [61–63]. Furthermore, the addition of a C═C adjacent to a C═O will bathochromically shift the $\pi \rightarrow \pi^*$ band into the visible region [64,65]. The "sweet, petrol-like" odor of the yellow liquid and λ_{max}= 269 nm point toward the presence of e.g., α, β-unsaturated acids, aldehydes, or aromatic hydrocarbons. Therefore, we believe the remaining, uncharacterized liquid to be a mixture of many trace molecules, including aromatic species, as evidenced by the small difference between HPLC-detected compounds and TOC (Fig. 11.A). This complexity makes direct comparison with individual reference compounds challenging, as the observed spectrum likely represents a composite of multiple absorbing species rather than a single compound.

Overall, it is interesting to consider that the formation of these oxygenates, e.g., formaldehyde, can be 'tailored' to some extent, according to the CO_2:CH_4 ratio (Fig. 10) and, given the selectivity data, formed in greater concentrations at lower pressure (i.e., < 500 mbar, Fig. 8.B and C). This suggests dual injection designs in MW-based plasma reactors can help to control temperature distributions, radical pathways, and thus product formation, such as for the production of oxygenates. The reader should note that the absolute concentrations at a given condition are subject to high uncertainties and further research is needed to accurately resolve the yields and potential for application; however, as a first approach, we made an approximation of the oxygenate production based on the available gas phase conversion, selectivity data, and liquid phase oxygenate concentrations. We take the 7:7 slm CO_2:CH_4 condition as an example, as it exhibits the highest measured oxygenate concentrations. As noted in *SI S.1*, these concentrations represent an average across all pressure and power data sets, encompassing a total of eight different conditions. As it has been typically reported in literature that the liquid by-product found in admixing DRM conditions is pure water, the experiment was not designed to make a distinction between conditions for the liquid fraction, and thus, is it not possible to quantify with accuracy, since one would need precise inflow and outflow quantities for a fixed data set.

As a first approximation, we assume that all missing oxygen in the oxygen balance (see *SI, S3.1, Table S.20*) can be attributed to H_2O formation, and thus we can have an estimation of the production rate of H_2O, given that the oxygenate concentrations are small compared to the H_2O fraction. Since CO and H_2O are the only dominate O-containing product species, each containing a single O atom, the H_2O production rate can be calculated by multiplying the CO_2 molar flow rate (F_{CO_2}) by the CO_2 conversion (X_{CO_2}) and the fraction of unidentified oxygen (S_O). To obtain the oxygenate production rate, we then multiply this value by the corresponding oxygenate concentration (c_{oxy}), resulting in the following expression for the approximated oxygenate production rate (PR_{oxy}):

$$PR_{oxy} = F_{CO_2} * X_{CO_2} * S_O * c_{oxy}$$

As the oxygenate concentrations represent averages, we also compute the average CO_2 conversion and unknown oxygen fraction across the different conditions. This yields an estimated average production rate of formaldehyde (2.1 μmol/s), acetic acid (0.7 μmol/s), and formic acid (0.1 μmol/s).

Our study's main research question was to establish a proof-of-concept for dual injection systems, where we identified (unexpected) oxygenate formation pathways that, in our opinion, warrant a dedicated investigation with more sophisticated multi-phase quantification protocols. Unfortunately, as this was not the initial goal of this study and given the data and the limitation of this configuration, we cannot provide accurate resolution of the temporal formation of the liquid fractions. Future work should focus on time-resolved analysis of all product phases to enable accurate mass balance closure and absolute production rate determination. We believe this is an interesting case for future work, especially because the industrial production of formaldehyde is very energy intensive [66,67], and it would be of interest to the community to know that we might be able to optimize the production of these valuable products in warm plasmas with carefully configured injection schemes for further progress toward electrification of the chemical industry.

In summary, dual injection with CH_4 as a reactive quenching agent in a DRM context presents some limitations for application. The low syngas ratios observed across all conditions result primarily from significant H_2O formation through the RWGS reaction, as confirmed by modeling. However, one important merit of the dual injection approach is that solid carbon formation is formed downstream of the discharge, mitigating instabilities associated with carbon coupling to the MW field when formed in the reactive volume. Thus, this approach successfully demonstrates that dual injection allows for higher CH_4 fractions without the plasma instability issues that typically occur with conventional admixing in DRM. Furthermore, the model predicts that at higher SEI and CH_4 ratios (240 kJ/mol, 1:4 CO_2: CH_4), we may yield increased syngas ratios (~2), discussed in detail in *SI, S.2.3*.

3.3. Carbon formation and morphology in a dual injection flow

To compare the carbon morphology from the dual injection flow (CO_2 plasma with CH_4 post-plasma injection) with conventional (admixing) DRM in MW plasma, as e.g., reported in *Kelly* et al. [42], we investigated the structure of the solid carbon collected from the walls of the viewing quartz and in the cyclone separator, observed to be formed at $p > 700$ mbar. Understanding the structure and morphology of the collected carbon can provide additional insight into the cooling rates using reactive post-plasma quenching. We again collected a carbon sample for each CO_2:CH_4 ratio and then treated it using the methods outlined in *SI, S.1.2,* to determine the structure. The deposits were characterized by SEM and TEM, revealing monodisperse samples (apart from one exception observed by TEM, see *SI, S.3.2*), and representative images are presented in Fig. 12.

Fig. 12.A and B show that agglomerates of sub-μm to several μm in size are observed in SEM, appearing to consist of many smaller particles, somewhat resembling a carbon black-like morphology [68]; however, the TEM analysis shows that the individual particles are, in fact, completely amorphous (Fig. 12.C and D). The amorphous structure of the material is confirmed by the high-magnification imaging and the Fast Fourier Transform (FFT) of this image (Fig. 12.D and the inset) revealing no spots or sharp rings in the FFT that would suggest the presence of local crystallinity. This indicates that the formed material is not carbon black, contrary to the carbon materials generated in conventional DRM in the same MW plasma reactor, including the work by *Kelly* et al. [42]. Furthermore, the seemingly individual particles observed by low-magnification imaging (Fig. 12.A and B) are completely fused together at the nanoscale (Fig. 12.C and D). Therefore, individual primary particles, as commonly defined for carbon black, cannot be readily described, thus preventing the definition of an average particle size for this material.

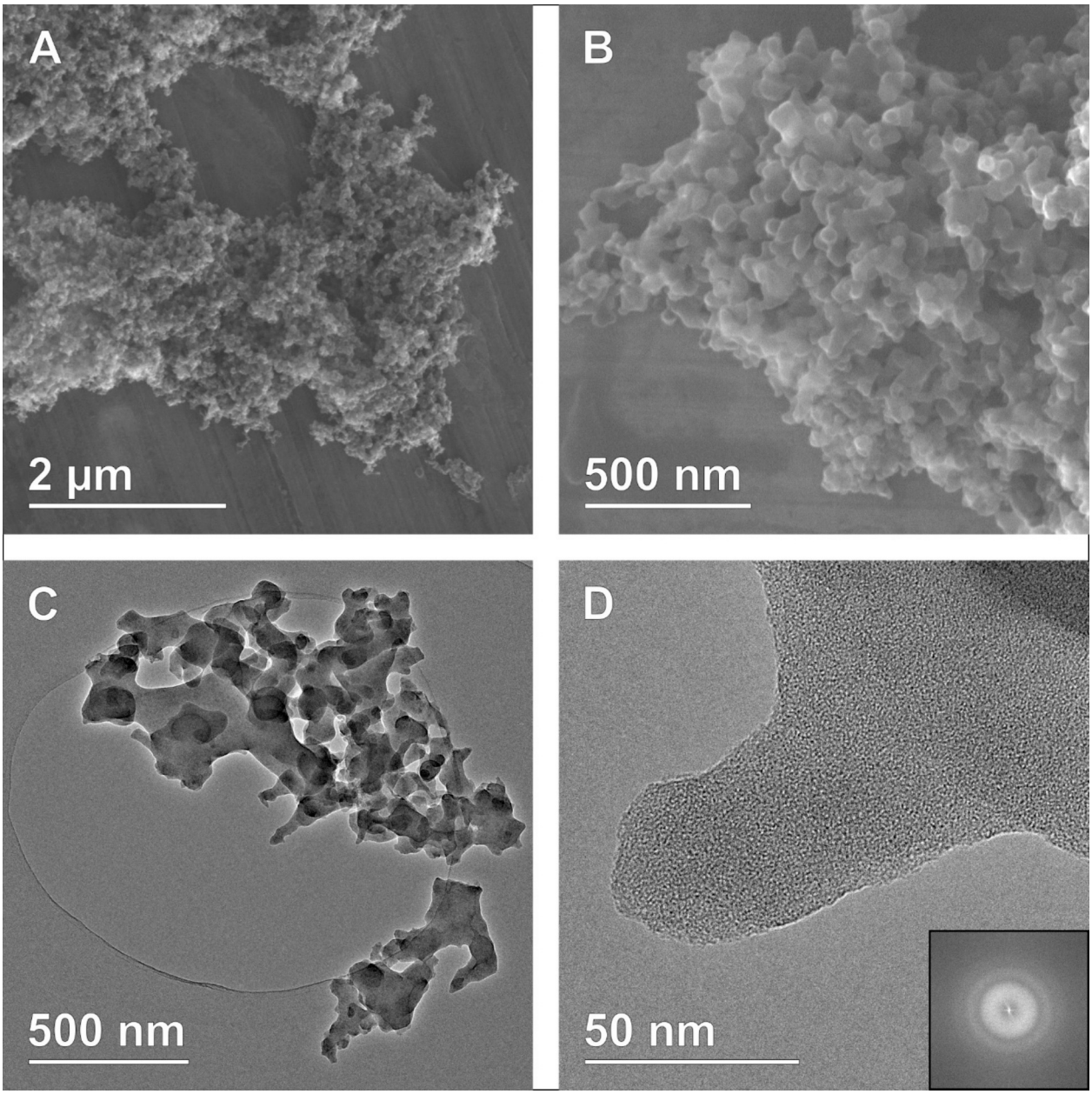

Fig. 12. A, B: SEM images of the deposited carbon materials, revealing large agglomerates, seemingly consisting of many smaller particles (see different scale bar in A and B). C, D: BF-TEM images of the deposited materials. The same morphology of agglomerated particles as found by SEM is observed, but higher magnification images (D) reveal that the particles are fused together, and the material is amorphous, confirmed by Fast Fourier Transform (as shown in the inset).

Studies have shown that the cooling rate plays a critical role in determining the crystallinity and structure of carbon materials formed during plasma-based carbon synthesis [51,69,70]. In the case of the fused amorphous carbon structures shown in Fig. 12.C and D, the post-plasma injection of CH_4 appears to significantly influence the final morphology. Determining the exact parameters of the cooling rate is not straightforward; however, as a first approximation, we consider the cooling rates determined by the 0D model. The model predicts the cooling rate of the total mixture upon CH_4 injection to be in the order of 10^5–10^6 K/s. We note that these values represent the global cooling rate of the simulated gas mixture, which is likely to be significantly lower than the microscopic cooling effects occurring over the length scale of particle diffusion. Literature studying carbon amorphous structures suggests rapid cooling rates trigger the transition to a more disordered morphology. For example, *Dozhdikov* et al. demonstrated that cooling rates between 10^{12} and 10^{14} K/s produce specific structural changes in carbon materials, with higher rates leading to more amorphous structures [71]. In the model developed by *Girshick* et al., very high cooling rates were shown to "freeze" carbon particles at smaller sizes because the temperature drops below the threshold where significant atomic rearrangement can occur [69]. Moreover, *Girshick* emphasizes two critical parameters, i.e., monomer concentration and cooling rate, and their influence on nucleation and growth of carbon particles in thermal plasma synthesis [69,72]. *Girshick* establishes that high monomer concentration and low cooling rates favor the nucleation of larger and fewer particles, whereas low monomer concentration and high cooling rates produce numerous smaller particles. According to *Girshick*, this relationship between nucleation rate and growth rate determines final particle morphology. In our case, the counter-flow CH_4 injection likely creates a high cooling rate, potentially diluting the carbon monomer concentration and pushing the system toward numerous small nuclei rather than organized growth.

Girshick also explains that particle formation occurs when supersaturation exceeds a critical threshold [69]. The counter-flow CH_4 injection likely creates a sharp supersaturation gradient that triggers rapid, uncontrolled nucleation throughout the secondary injection region, rather than sequential growth on existing nuclei, as we might find with carbon particles formed around the reactive volume near the plasma in the case of DRM, i.e., when CO_2 and CH_4 are admixed [42]. *Fabry* et al. also reports that internal mixing, or recirculation cells, significantly affect particle structure [51]. The counter-flow secondary injection of CH_4 is designed to enhance mixing conditions, likely creating a complex flow pattern where the CH_4 counter-flow would disrupt the carbon aggregation process normally found in plasma-based admixing dissociation of CH_4. If the counter-flow injection of CH_4 created an extreme local temperature gradient, as would be expected, carbon precursors would solidify before they could organize into the typical spheroidal primary carbon particles, as previously reported by *Kelly* et al [42]. This may explain the completely fused, amorphous structure observed in the TEM images shown in Fig. 12.D.

The amorphous structure represents an interesting morphological state outside of typical plasma-generated carbon materials found in literature [41,42,51,52,73–75]. In our dual injection system, the particles appear to have undergone partial coagulation, forming the agglomerated structure seen in Fig. 12.D, lacking the energy for surface reorganization that would normally occur in carbon black formation, resulting in completely fused interfaces between particles. Likely, a rapid temperature drop from the counterflow injection of CH_4 into the afterglow region "freezes" the carbon in an amorphous state before proper nucleation, growth, and graphitization can occur, resulting in the fused, completely amorphous morphology observed in the TEM images (Fig. 12.C and D) [69,76].

We also note that in our dual injection system, no carbon formation was observed in the afterglow viewing quartz below $p = 700$ mbar. *Fabry* et al. discusses the thermodynamic equilibrium of the C—H system and how carbon formation has specific pressure and temperature requirements [51]. Additionally, the reactions leading to carbon formation typically involve multiple collision steps [51,68,76]. Below 700 mbar, the mean free path increases, reducing collision frequency, which affects the kinetics of carbon formation, potentially shifting reaction pathways toward other products. This suggests that pressure affects the balance between different reaction pathways, where the selectivity of carbon species will shift toward gaseous products (such as C_xH_y, CO) or to oxygenate formation, as discussed in Section 3.2, rather than condensing into solid carbon. Finally, at lower pressures, the interaction between the CO_2 plasma afterglow and reactive quenching of CH_4 may change significantly. The pressure threshold of 700 mbar might represent a critical point where flow dynamics create appropriate mixing conditions for carbon agglomeration/coagulation, suggesting a minimum pressure environment is needed to achieve the necessary supersaturation, residence time, and reaction kinetics for carbon nucleation and growth in a dual injection plasma system. Our findings suggest that pressure may affect the nucleation kinetics or shift the selectivity in dual injection plasma systems. However, given the large unknown fraction of C atoms in the selectivity data, we believe that there may be carbon nucleation still present that is not able to coagulate, and is not detectable in the post-reactive volume (i.e., in the viewing quartz), nor would it be collected in the cyclone separator, which is limited to particles down to 1 μm with 95 % efficiency.

Amorphous carbon can exhibit valuable properties for specific applications; however, the characterization of the carbon materials in this study serves primarily to provide insights into the cooling dynamics of the reactive quenching process rather than to optimize carbon as a product. Nevertheless, it is worth noting that amorphous carbon materials can find applications in various fields depending on their specific morphological and structural characteristics. For instance, highly porous amorphous carbons with large surface areas are valuable for energy storage applications such as supercapacitors and battery electrodes [77], while dense, non-porous amorphous carbons may be suitable for protective coatings or as reinforcement materials [78,79]. The fused, completely amorphous morphology observed in our study (Fig. 12.C and D) suggests a dense, low-porosity structure that would likely be more suitable for applications requiring mechanical strength rather than high surface area applications [80]. However, a comprehensive characterization of properties such as surface area, porosity, electrical conductivity, and mechanical properties would be necessary to fully assess the potential applications of these materials. Since the agglomeration into amorphous solid carbon formation represents only a minor fraction of our products and appears to occur only at higher pressures ($p > 700$ mbar), our primary focus remains on understanding how the carbon morphology reflects the underlying rapid cooling mechanisms inherent to the dual injection approach.

4. Conclusions and future work

We investigated the effects of dual injection in a 2.45 GHz CO_2 MW plasma system, where CH_4 was strategically injected as a reactive quenching agent into the high-temperature post-plasma afterglow region. Our findings provide novel insights into how this configuration affects conversion, product selectivity, as well as liquid and carbon formation.

The introduction of CH_4 in the post-plasma region demonstrates approximately a threefold increase in absolute CO_2 conversion compared to pure CO_2 plasma, reaching consistent values of ~28 % at 1000 W and 10 slm primary CO_2 flow rate, for different secondary CH_4 flow rates and across the entire investigated pressure range from 200 to 900 mbar. This pressure-independent behavior suggests that post-plasma CH_4 injection effectively mitigates the recombination processes that typically limit CO_2 conversion at higher pressures, which is also convincingly predicted by our model as the RWGS reaction does not show strong pressure dependence. Overall, reactive quenching with CH_4 appears to be more effective at higher *SEI* input, and when the flow rate

of the secondary injection (CH_4) is less than the flow rate of the primary injection (CO_2). It would be of interest to further explore the parameter space to enhance the CO_2 conversion with reactive quenching. In all the data collected, no characteristic H_α emission was observed to indicate upstream migration of CH_4 into the discharge zone, confirming that the secondary injection remained confined to the afterglow region (see *SI, S.1.3* for additional details). We believe this is likely due to the distance of the secondary injection inlet, or perhaps a suboptimal design profile of the secondary tangential injection. This opens the possibility for future studies to explore alternative injection profiles, such as ring injection geometries, to enhance mixing and potentially to allow for controlled upstream interaction between CH_4 and the plasma volume. Furthermore, investigating the effects of reducing the distance between the secondary injection and the waveguide may help determine the optimal positioning for maximum conversion of both reactive gases while maintaining plasma stability.

The highest CO_2 and CH_4 conversion (55 % and 37 %, respectively) is achieved at 500 mbar for the 7:7 slm, CO_2:CH_4 ratio at 1250 W, i.e., higher *SEI* conditions, under which solid carbon formation is not observed as an irradiated plume nor does it collect along the quartz walls in the secondary viewing quartz. Furthermore, our study reveals that the limited carbon formed at higher pressures (as shown in the selectivity analysis) exhibits an unusual fused amorphous morphology, distinctly different from the spheroidal carbon black particles typically formed during traditional admixed DRM conversion. This atypical morphology is attributed to the high cooling rates (likely $> \sim 10^6$ K/s) created by the counter-flow injection of CH_4, which produces carbon in an amorphous state.

While the dual injection approach improves CO_2 conversion, the syngas ratio shows a maximum H_2:CO ratio of only 0.37 at quasi-atmospheric pressure, and our modeling reveals that the low syngas ratios are likely due to the relatively low *SEI* applied in this work (due to power supply limitations). This low syngas ratio is attributed to significant H_2O formation, confirmed through our 0D kinetic model analysis. The model revealed that when CH_4 is injected as a reactive quenching agent under limited *SEI* conditions, partial oxidation of CH_4 by O_2/O radicals generated in the CO_2 discharge proceeds rapidly, and the resulting H atoms react with CO_2 to form CO and OH radicals. The reactive mixture quickly relaxes to the RWGS equilibrium, leading to further CO_2 conversion and ultimately producing H_2O. As temperatures rapidly decrease below 2000 K, these reactions become kinetically limited, preventing H_2 reformation and increasing the final H_2O concentration. Given the fast kinetics of the RWGS reaction, suppressing H_2O formation by manipulating the rate of CH_4 addition or the cooling trajectory may be very challenging to achieve in practical applications. Moreover, actively cooling the system to temperatures where partial oxidation of CH_4 remains feasible but RWGS kinetics are effectively frozen would not be an effective strategy, as it would result in low CH_4 conversion. Indeed, the fraction of oxygen available in the CO_2 plasma effluent is inherently limited. Once all available oxygen is consumed in the partial oxidation of CH_4, maintaining high mixture temperatures remains essential to facilitate the reforming process. Experiments using isotopically labeled $^{13}CH_4$ or H_2 would be of interest to confirm additional CO formation through the RWGS reaction. Furthermore, our model predicts that a higher SEI will likely yield higher H_2 selectivity and syngas ratios, which could be of interest to future research initiatives.

Therefore, we argue that injecting all CH_4 as close to the discharge (at the end of the waveguide) as possible, coupled with reactor isolation, is the optimal strategy for maximizing the residual CO_2 plasma heat in the reforming process. This approach eliminates the need for alternative strategies such as staged CH_4 addition or temperature-buffered zones. Moreover, higher CO_2 conversion will lead to lower H_2O concentrations, following the constraints imposed by the RWGS equilibrium. As a result, this mechanism would enhance H_2 selectivity and likely improve the syngas ratio. At the SEI used in this study (a limitation of our reactor's maximum power output), the residual heat following CO_2 discharge is insufficient to sustain significant DRM chemistry. The effective *SEI* values applied (< 132 kJ/mol) are relatively low compared to optimal conditions reported in other DRM studies; however, to avoid impractically high power-to-CO_2 flow rate ratios in the CO_2 discharge, total energy input could be enhanced through methods such as preheating of the CO_2 and CH_4 streams, ideally via heat recovery, which would further improve energy efficiency. Since maintaining elevated temperatures during post-plasma conversion is crucial for optimizing performance, minimizing thermal losses by insulating the reactor could provide additional benefits. Research involving preheating the primary injection gas to help reduce the *SEI* to the discharge gas may prove to be an advantageous strategy to increase conversion of both reactants.

Importantly, this work demonstrates that dual injection configurations are promising for enhancing CO_2 conversion while minimizing or eliminating carbon deposition, a significant challenge in conventional plasma-based DRM. Moreover, larger fractions of CH_4 can be treated with post-plasma injection. Future research should focus on refining the injection location, increasing the *SEI* to the discharge gas, and developing reactor designs that enhance mixing dynamics to control product selectivity more precisely. The liquid product analysis identified formaldehyde, acetic acid, and formic acid as the primary oxygenates formed during the process, with the highest concentrations observed in the samples with a 7:7 slm, CO_2:CH_4 ratio. UV–Vis spectroscopy revealed a $\lambda_{max} = 269$ nm, suggesting the presence of trace molecules with conjugated systems. These findings indicate that dual injection can potentially be optimized for selective oxygenate production, particularly at sub-atmospheric pressures, where selectivity analysis suggests higher concentrations are likely to form. Additionally, further investigation of the pressure-dependent carbon nucleation and coagulation mechanisms could provide valuable insights for designing carbon-free plasma conversion systems or tailoring to higher value molecules (e.g., oxygenates).

Our experimental data reveals significant insights into the complex interplay between plasma dynamics, flow geometry, reaction thermodynamics, and carbon deposition behavior when introducing CH_4 as a reactive quenching agent. While our results demonstrate proof-of-concept benefits, including enhanced CO_2 conversion, we recognize that the current performance metrics present significant challenges for industrial scale-up. Several key challenges must be addressed before considering industrial scaling of a dual injection system, including understanding how spatial delivery and injection geometry may affect mixing and upstream interactions, which are important factors in larger-scale reactors. Furthermore, changes to these aspects of the process may affect temperature gradients and cooling rates, which may change product selectivity and kinetic pathways. We also believe it would be of great interest to the community to further understand the potential for warm plasma based oxygenate production through targeted studies with dual injection systems. Understanding this is crucial for realizing additional avenues for electrification of the chemical industry using MW plasma technology.

Therefore, further optimization studies, with for example, higher *SEI* conditions, altering the injection geometry, as well as investigating changes to product distribution with injection position, are necessary to understand the industrial potential, as the energy cost and syngas ratios are far below what would be interesting for industrial applications. Although our modeling work suggests that higher *SEI* may improve these metrics, experimental validation is needed, which may require substantial process redesign; however, we believe that the primary value of this work lies in advancing fundamental understanding of plasma-based reactive quenching mechanisms rather than immediate commercial application. The insights gained regarding oxygen scavenging mechanisms and product selectivity shifts with pressure provide a foundation for future research directions. These findings not only advance our understanding of plasma-based DRM mechanisms but also provide practical guidance for optimizing process engineering and operation parameters. By leveraging the thermal energy of the plasma afterglow

through strategic reactive quenching, this approach represents a step toward more precise control of plasma chemistry and potentially opens new pathways for the selective production of fuels and chemicals from greenhouse gases, contributing to the development of carbon-circular economy technologies.

CRediT authorship contribution statement

E.R. Mercer: Writing – original draft, Visualization, Software, Methodology, Investigation, Formal analysis, Data curation, Conceptualization. **M. Albrechts** Writing – original draft, Visualization, Software, Methodology, Investigation, Formal analysis, Data curation. **R. De Meyer:** Writing – original draft, Investigation, Data curation. **I. Fedirchyk:** Writing – original draft, Investigation. **E. Morais:** Writing – review & editing. **S. Bals:** Supervision, Resources, Funding acquisition. **A. Bogaerts:** Writing – review & editing, Supervision, Resources, Funding acquisition.

Funding

This research was supported by the European Research Council (ERC) under the European Union's Horizon 2020 Research and Innovation Program (grant agreement No 810182 – SCOPE ERC Synergy project).

Declaration of competing interest

The authors declare that they have no known competing financial interests or personal relationships that could have appeared to influence the work reported in this paper.

Acknowledgments

We would like to acknowledge the contribution of the research group Applied Electrochemistry & Catalysis (ELCAT) in the Faculty of Applied Engineering at UAntwerpen, and particularly Max Van Brusselen and Thomas Kenis for their invaluable support during the liquid analysis. We would also like to acknowledge the work of Helder Van Poyer in collecting the baseline measurements for CO_2 conversion, as well as the support of Dr. Bart Wanten both during our experimental investigation and in the extensive analysis of the results. Furthermore, we extend our sincere gratitude to the machine shop at the University of Antwerp, whose exceptional craftsmanship and technical expertise were instrumental in bringing our experimental designs to life. Their precision, innovation, and dedication in fabricating the custom components were vital to the success of this research project.

Appendix A. Supplementary data

Supplementary data to this article can be found online at https://doi.org/10.1016/j.cej.2025.166038.

Data availability

Data will be made available upon request.

References

[1] IRENA, Renewable Energy Statistics 2024, International Renewable Energy Agency, 2024.
[2] I.E.A. (IEA), Direct CO2 emissions from primary chemical production in the Net Zero Scenario, 2010–2030, in: L.C. D'iana Perex Sanchez, Fabian Voswinkel (Ed.), 2023.
[3] W. Bongers, H. Bouwmeester, B. Wolf, F. Peeters, S. Welzel, D. van den Bekerom, N. den Harder, A. Goede, M. Graswinckel, P.W. Groen, Plasma-driven dissociation of CO_2 for fuel synthesis, Plasma Process. Polym. 14 (6) (2017) 1600126, https://doi.org/10.1002/ppap.201600126.
[4] A.P. Goede, W.A. Bongers, M.F. Graswinckel, R.M. van de Sanden, M. Leins, J. Kopecki, A. Schulz, M. Walker, Production of solar fuels by CO_2 plasmolysis, EPJ Web Conf. (2014) 01005. EDP Sciences.
[5] R. Snoeckx, A. Bogaerts, Plasma technology – a novel solution for CO2 conversion? Chem. Soc. Rev. 46 (19) (2017) 5805–5863, https://doi.org/10.1039/C6CS00066E.
[6] S. Mehariya, A. Iovine, P. Casella, D. Musmarra, A. Figoli, T. Marino, N. Sharma, A. Molino, Chapter 7 - Fischer–Tropsch synthesis of syngas to liquid hydrocarbons, in: A. Yousuf, D. Pirozzi, F. Sannino (Eds.), Lignocellulosic Biomass to Liquid Biofuels, Academic Press, 2020, pp. 217–248, https://doi.org/10.1016/B978-0-12-815936-1.00007-1.
[7] A. Hecimovic, F.A. D'Isa, E. Carbone, U. Fantz, Enhancement of CO2 conversion in microwave plasmas using a nozzle in the effluent, J CO_2 Util 57 (2022) 101870, https://doi.org/10.1016/j.jcou.2021.101870.
[8] A. Hecimovic, C.K. Kiefer, A. Meindl, R. Antunes, U. Fantz, Fast gas quenching of microwave plasma effluent for enhanced CO2 conversion, J CO_2 Util 71 (2023) 102473, https://doi.org/10.1016/j.jcou.2023.102473.
[9] J. Li, X. Zhang, J. Shen, T. Ran, P. Chen, Y. Yin, Dissociation of CO2 by thermal plasma with contracting nozzle quenching, J CO_2 Util 21 (2017) 72–76, https://doi.org/10.1016/j.jcou.2017.04.003.
[10] E.R. Mercer, S. Van Alphen, C.F.A.M. van Deursen, T.W.H. Righart, W.A. Bongers, R. Snyders, A. Bogaerts, M.C.M. van de Sanden, F.J.J. Peeters, Post-plasma quenching to improve conversion and energy efficiency in a CO_2 microwave plasma, Fuel 334 (2023) 126734, https://doi.org/10.1016/j.fuel.2022.126734.
[11] M.Y. Ong, S. Nomanbhay, F. Kusumo, P.L. Show, Application of microwave plasma technology to convert carbon dioxide (CO2) into high value products: a review, J. Clean. Prod. 336 (2022) 130447, https://doi.org/10.1016/j.jclepro.2022.130447.
[12] A. van de Steeg, P. Viegas, A. Silva, T. Butterworth, A. van Bavel, J. Smits, P. Diomede, M. van de Sanden, G. van Rooij, Redefining the microwave plasma-mediated CO_2 reduction efficiency limit: the role of o–CO_2 association, ACS Energy Lett. 6 (8) (2021) 2876–2881, https://doi.org/10.1021/acsenergylett.1c01206.
[13] D.C.M. van den Bekerom, J.M.P. Linares, T. Verreycken, E.M. van Veldhuizen, S. Nijdam, G. Berden, W.A. Bongers, M.C.M. van de Sanden, G.J. van Rooij, The importance of thermal dissociation in CO2 microwave discharges investigated by power pulsing and rotational Raman scattering, Plasma Sources Science and Technology 28 (5) (2019) 055015, https://doi.org/10.1088/1361-6595/aaf519.
[14] C. van Deursen, H. Van Poyer, W. Bongers, F. Peeters, F. Smits, M. van de Sanden, Effluent nozzles in reverse-vortex-stabilized microwave CO_2 plasmas for improved energy efficiency, J. CO2 Util. 88 (2024) 102952, https://doi.org/10.1016/j.jcou.2024.102952.
[15] A.J. Wolf, F. Peeters, P. Groen, W. Bongers, Van De M. Sanden, CO_2 conversion in nonuniform discharges: disentangling dissociation and recombination mechanisms, J. Phys. Chem. C 124 (31) (2020) 16806–16819, https://doi.org/10.1021/acs.jpcc.0c03637.
[16] A.J. Wolf, T.W. Righart, F. Peeters, W. Bongers, Van De M. Sanden, Implications of thermo-chemical instability on the contracted modes in CO2 microwave plasmas, Plasma Sources Sci. Technol. 29 (2) (2020) 025005, https://doi.org/10.1088/1361-6595/ab5eca.
[17] A. Berthelot, A. Bogaerts, Modeling of CO2 splitting in a microwave plasma: how to improve the conversion and energy efficiency, J. Phys. Chem. C 121 (15) (2017) 8236–8251.
[18] C.K. Kiefer, R. Antunes, A. Hecimovic, A. Meindl, U. Fantz, CO2 dissociation using a lab-scale microwave plasma torch: an experimental study in view of industrial application, Chem. Eng. J. 481 (2024) 148326, https://doi.org/10.1016/j.cej.2023.148326.
[19] A. Van de Steeg, L. Vialetto, A. S. d Silva, P. Viegas, P. Diomede, M. Van de Sanden, G. Van Rooij, The chemical origins of plasma contraction and thermalization in CO_2 microwave discharges, J. Phys. Chem. Lett. 13 (5) (2022) 1203–1208, https://doi.org/10.1021/acs.jpclett.1c03731.
[20] K. Wang, S. Ceulemans, H. Zhang, I. Tsonev, Y. Zhang, Y. Long, M. Fang, X. Li, J. Yan, A. Bogaerts, Inhibiting recombination to improve the performance of plasma-based CO2 conversion, Chem. Eng. J. 481 (2024) 148684, https://doi.org/10.1016/j.cej.2024.148684.
[21] L. Vialetto, A.W. van de Steeg, P. Viegas, S. Longo, G.J. van Rooij, M.C.M. van de Sanden, J. van Dijk, P. Diomede, Charged particle kinetics and gas heating in CO2 microwave plasma contraction: comparisons of simulations and experiments, Plasma Sources Science and Technology 31 (5) (2022) 055005, https://doi.org/10.1088/1361-6595/ac56c5.
[22] R. Vertongen, I. Tsonev, A. Bogaerts, Enhancing CO2 conversion with gas quenching in arc plasma, Chem. Eng. J. 505 (2025) 159487, https://doi.org/10.1016/j.cej.2025.159487.
[23] G. Raposo, A.W. van de Steeg, E.R. Mercer, C.F.A.M. van Deursen, H.J. L. Hendrickx, W.A. Bongers, G.J. van Rooij, M.C.M. van de Sanden, F.J.J. Peeters, Flame bands: CO + O chemiluminescence as a measure of gas temperature, J. Phys. D Appl. Phys. 54 (37) (2021) 374005, https://doi.org/10.1088/1361-6463/ac0924.
[24] M. Albrechts, I. Tsonev, A. Bogaerts, Can post-plasma CH4 injection improve plasma-based dry reforming of methane? A modeling study, Green Chem. 26 (18) (2024) 9712–9728, https://doi.org/10.1039/D4GC02889A.
[25] J. Slaets, E. Morais, A. Bogaerts, Afterglow quenching in plasma-based dry reforming of methane: a detailed analysis of the post-plasma chemistry via kinetic modelling, RSC Sustainability 3 (3) (2025) 1477–1493, https://doi.org/10.1039/D4SU00676C.

[26] V. Vermeiren, A. Bogaerts, Plasma-based CO2 conversion: to quench or not to quench? J. Phys. Chem. C 124 (34) (2020) 18401–18415, https://doi.org/10.1021/acs.jpcc.0c04257.

[27] R. Vertongen, G. Trenchev, R. Van Loenhout, A. Bogaerts, Enhancing CO2 conversion with plasma reactors in series and O2 removal, J CO_2 Util 66 (2022) 102252, https://doi.org/10.1016/j.jcou.2022.102252.

[28] F. Girard-Sahun, O. Biondo, G. Trenchev, G. van Rooij, A. Bogaerts, Carbon bed post-plasma to enhance the CO2 conversion and remove O2 from the product stream, Chem. Eng. J. 442 (2022) 136268, https://doi.org/10.1016/j.cej.2022.136268.

[29] O. Biondo, K. Wang, H. Zhang, A. Bogaerts, Coupling a CO2 plasma with a carbon bed: the closer the better, Chem. Eng. J. 507 (2025) 160190, https://doi.org/10.1016/j.cej.2025.160190.

[30] C. O'Modhrain, Y. Gorbanev, A. Bogaerts, Post-plasma carbon bed design for CO2 conversion: does size and insulation matter? journal of energy Chemistry 104 (2025) 312–323, https://doi.org/10.1016/j.jechem.2024.12.066.

[31] H. Zhang, Q. Tan, Q. Huang, K. Wang, X. Tu, X. Zhao, C. Wu, J. Yan, X. Li, Boosting the conversion of CO2 with biochar to clean CO in an atmospheric Plasmatron: a synergy of plasma chemistry and thermochemistry, ACS Sustainable Chemistry & Engineering 10 (23) (2022) 7712–7725, https://doi.org/10.1021/acssuschemeng.2c01778.

[32] G. Van Rooij, H. Akse, W. Bongers, M. Van De Sanden, Plasma for electrification of chemical industry: a case study on CO_2 reduction, Plasma Phys. Controlled Fusion 60 (1) (2017) 014019, https://doi.org/10.1088/1361-6587/aa8f7d.

[33] N.V. Chekmarev, D.A. Mansfeld, A.V. Vodopyanov, S.V. Sintsov, E. I. Preobrazhensky, M.A. Remez, Enhancement of CO2 conversion by counterflow gas quenching of the post-discharge region in microwave plasma sustained by gyrotron radiation, J CO_2 Util 82 (2024) 102759, https://doi.org/10.1016/j.jcou.2024.102759.

[34] D. Mansfeld, S. Sintsov, N. Chekmarev, A. Vodopyanov, Conversion of carbon dioxide in microwave plasma torch sustained by gyrotron radiation at frequency of 24 GHz at atmospheric pressure, J CO_2 Util 40 (2020) 101197, https://doi.org/10.1016/j.jcou.2020.101197.

[35] N.V. Chekmarev, D.A.e. Mansfeld, E.I. Preobrazhensky, S.V. Sintsov, M. Remez, A. V. Vodopyanov, Suppression of reverse reactions during carbon dioxide decomposition in microwave discharge plasma, Pis'ma Zh. Tekh. Fiz. 49 (24) (2023) 31–34.

[36] R. Aerts, R. Snoeckx, A. Bogaerts, In-situ chemical trapping of oxygen in the splitting of carbon dioxide by plasma, Plasma Process. Polym. 11 (10) (2014) 985–992, https://doi.org/10.1002/ppap.201400091.

[37] Y. Liu, E. Hu, E.A. Khan, Z. Lai, Synthesis and characterization of ZIF-69 membranes and separation for CO2/CO mixture, J. Membr. Sci. 353 (1) (2010) 36–40, https://doi.org/10.1016/j.memsci.2010.02.023.

[38] A. Brunetti, F. Scura, G. Barbieri, E. Drioli, Membrane technologies for CO2 separation, J. Membr. Sci. 359 (1) (2010) 115–125, https://doi.org/10.1016/j.memsci.2009.11.040.

[39] O. Biondo, A. Hughes, A. van de Steeg, S. Maerivoet, B. Loenders, G. van Rooij, A. Bogaerts, Power concentration determined by thermodynamic properties in complex gas mixtures: the case of plasma-based dry reforming of methane, Plasma Sources Sci. Technol. 32 (4) (2023) 045001, https://doi.org/10.1088/1361-6595/acc6ec.

[40] O. Biondo, C.F. Van Deursen, A. Hughes, A. van de Steeg, W. Bongers, M. van de Sanden, G. van Rooij, A. Bogaerts, Avoiding solid carbon deposition in plasma-based dry reforming of methane, Green Chem. 25 (24) (2023) 10485–10497.

[41] C. Hyun Cho, J.H. Kim, J.K. Yang, I.S. Park, Y.-S. Choi, I.J. Kang, Dry reforming process using microwave plasma generator with high carbon dioxide conversion efficiency for syngas production, Fuel 361 (2024) 130707, https://doi.org/10.1016/j.fuel.2023.130707.

[42] S. Kelly, E. Mercer, R. De Meyer, R.-G. Ciocarlan, S. Bals, A. Bogaerts, Microwave plasma-based dry reforming of methane: reaction performance and carbon formation, J CO_2 Util 75 (2023) 102564, https://doi.org/10.1016/j.jcou.2023.102564.

[43] M.I. Malik, I.E. Achouri, N. Abatzoglou, F. Gitzhofer, Intensified performance of methane dry reforming based on non-thermal plasma technology: recent progress and key challenges, Fuel Process. Technol. 245 (2023) 107748, https://doi.org/10.1016/j.fuproc.2023.107748.

[44] H. Sun, J. Lee, M.S. Bak, Experiments and modeling of atmospheric pressure microwave plasma reforming of a methane-carbon dioxide mixture, J CO_2 Util 46 (2021) 101464, https://doi.org/10.1016/j.jcou.2021.101464.

[45] B. Wanten, Dry, Bi-and Oxidative CO2 Reforming of CH4 in an Atmospheric Pressure Glow Discharge Reactor: An Experimental Study, University of Antwerp, 2024.

[46] B. Wanten, Y. Gorbanev, A. Bogaerts, Plasma-based conversion of CO2 and CH4 into syngas: a dive into the effect of adding water, Fuel 374 (2024) 132355.

[47] B. Wanten, S. Maerivoet, C. Vantomme, J. Slaets, G. Trenchev, A. Bogaerts, Dry reforming of methane in an atmospheric pressure glow discharge: confining the plasma to expand the performance, J CO_2 Util 56 (2022) 101869.

[48] S. Van Alphen, B. Wanten, F. Girard-Sahun, J. Slaets, J. Creel, M. Aghaei, A. Bogaerts, The role of CH4 in plasma-assisted CO2 and CH4 conversion in a rotating gliding arc plasma: insights revealed by experiments and modeling, ACS Sustainable Chemistry & Engineering 12 (42) (2024) 15715–15728.

[49] S. Maerivoet, B. Wanten, R. De Meyer, M. Van Hove, S. Van Alphen, A. Bogaerts, Effect of O2 on plasma-based dry reforming of methane: revealing the optimal gas composition via experiments and modeling of an atmospheric pressure glow discharge, ACS Sustain. Chem. Eng. 12 (30) (2024) 11419–11434.

[50] J.A. Menéndez, A. Arenillas, B. Fidalgo, Y. Fernández, L. Zubizarreta, E.G. Calvo, J. M. Bermúdez, Microwave heating processes involving carbon materials, Fuel Process. Technol. 91 (1) (2010) 1–8, https://doi.org/10.1016/j.fuproc.2009.08.021.

[51] F. Fabry, G. Flamant, L. Fulcheri, Carbon black processing by thermal plasma. Analysis of the particle formation mechanism, Chem. Eng. Sci. 56 (6) (2001) 2123–2132.

[52] R. Pristavita, N.-Y. Mendoza-Gonzalez, J.-L. Meunier, D. Berk, Carbon blacks produced by thermal plasma: the influence of the reactor geometry on the product morphology, Plasma Chemistry and Plasma Processing 30 (2010) 267–279.

[53] J.M. Coulson, Coulson & Richardson's Chemical engineering, in: J.M. Coulson, J. F. Richardson, R.K. Sinnott (Eds.), Chemical Engineering Design, 3rd ed. Vol. 6, Oxford: Butterworth-Heinemann, Oxford, 1999.

[54] B. Wanten, R. Vertongen, R. De Meyer, A. Bogaerts, Plasma-based CO2 conversion: how to correctly analyze the performance? J. Energy Chem. 86 (2023) 180–196, https://doi.org/10.1016/j.jechem.2023.07.005.

[55] COMSOL Multiphysics®.

[56] D.M.G. Gregory P. Smith, Michael Frenklach, Nigel W. Moriarty, Boris Eiteneer, Mikhail Goldenberg, C. Thomas Bowman, Ronald K. Hanson, Soonho Song, William C. Gardiner, Jr., Vitali V. Lissianski, and Zhiwei Qin, GRI-Mech 3.0.

[57] I.P. Butylkin, V.K. Zhivotov, E.G. Krasheninnikov, M.F. Krotov, V.D. Rusanov, I. V. Tarasov, A.A. Fridman, Plasma-chemical process of CO2 dissociation in a nonequilibrium microwave discharge, Zh. Tekh. Fiz. 51 (1981) 925–931.

[58] H. Kim, S. Song, C.P. Tom, F. Xie, Carbon dioxide conversion in an atmospheric pressure microwave plasma reactor: improving efficiencies by enhancing afterglow quenching, J CO_2 Util 37 (2020) 240–247, https://doi.org/10.1016/j.jcou.2019.12.011.

[59] K. Hiraoka, T. Sato, S. Sato, N. Sogoshi, T. Yokoyama, H. Takashima, S. Kitagawa, Formation of formaldehyde by the tunneling reaction of H with solid CO at 10 K revisited, Astrophys. J. 577 (1) (2002) 265, https://doi.org/10.1086/342132.

[60] W.D. Watson, Interstellar chemistry, Acc. Chem. Res. 10 (6) (1977) 221–226, https://doi.org/10.1021/ar50114a005.

[61] M.R. Leonardo, L.A.B. da Silva, M.T. Filho, R.S. da Silva, Release of formaldehyde by 4 endodontic sealers, Oral Surg. Oral Med. Oral Pathol. Oral Radiol. Endod. 88 (2) (1999) 221–225, https://doi.org/10.1016/S1079-2104(99)70119-8.

[62] S. Lee, H. Ju, H. Jeon, R.L. Machunda, D. Kim, J.K. Lee, J. Lee, Electrocatalytic reduction of gas-phased CO2 on nano-sized Sn electrode surface, ECS Trans. 53 (29) (2013) 41, https://doi.org/10.1149/05329.0041ecst.

[63] G. Ruderman, E.R. Caffarena, I.G. Mogilner, E.J. Tolosa, Hydrogen bonding of carboxylic acids in aqueous solutions—UV spectroscopy, viscosity, and molecular simulation of acetic acid, J. Solution Chem. 27 (10) (1998) 935–948, https://doi.org/10.1023/A:1022615329598.

[64] S. Ghosh, S. Nandi, A Comprehensive Review on UV-Visible Spectroscopy and Its application.

[65] H.-H. Perkampus, UV-VIS Spectroscopy and its Applications, Springer Science & Business Media, 2013.

[66] J. Puhar, A. Vujanović, P. Awad, L. Čuček, Reduction of cost, energy and emissions of the formalin production process via methane steam reforming, Systems 9 (1) (2021) 5.

[67] C.J. Sebastian, F.N. Adhyaksa, M.T. Kamal, V.E. Susanto, Optimization of energy consumption in formaldehyde production process using reboiled absorption process, Journal of Chemical Engineering Research Progress (2024) 13, https://doi.org/10.9767/jcerp.20094.

[68] J.-B. Donnet, Carbon Black: Science and Technology. Routledge, 2018.

[69] S.L. Girshick, C.P. Chiu, Homogeneous nucleation of particles from the vapor phase in thermal plasma synthesis, Plasma Chem. Plasma Process. 9 (3) (1989) 355–369, https://doi.org/10.1007/BF01083672.

[70] T.W. Zerda, W. Xu, H. Yang, M. Gerspacher, The effects of heating and cooling rates on the structure of carbon black particles, Rubber Chem. Technol. 71 (1) (1998) 26–37, https://doi.org/10.5254/1.3538469.

[71] V. Dozhdikov, A.Y. Basharin, P. Levashov, Structure studies of graded amorphous carbon obtained by liquid carbon quenching, Tech. Phys. 69 (5) (2024) 1170–1180.

[72] S.L. Girshick, C.-P. Chiu, P.H. McMurry, Modelling particle formation and growth in a plasma synthesis reactor, Plasma Chemistry and Plasma Processing 8 (2) (1988) 145–157, https://doi.org/10.1007/BF01016154.

[73] M. Gautier, V. Rohani, L. Fulcheri, Direct decarbonization of methane by thermal plasma for the production of hydrogen and high value-added carbon black, Int. J. Hydrogen Energy 42 (47) (2017) 28140–28156.

[74] X.-F. Guo, G.-J. Kim, Synthesis of ultrafine carbon black by pyrolysis of polymers using a direct current thermal plasma process, Plasma Chemistry and Plasma Processing 30 (2010) 75–90.

[75] L. Juan, H. Fangfang, L. Yiwen, Y. Yongxiang, D. Xiaoyan, X. Liao, A new grade carbon black produced by thermal plasma process, Plasma Sci. Technol. 5 (3) (2003) 1815.

[76] R.O. Grisdale, The formation of black carbon, J. Appl. Phys. 24 (9) (1953) 1082–1091, https://doi.org/10.1063/1.1721452.

[77] D.R. Lobato-Peralta, P.U. Okoye, C. Alegre, A review on carbon materials for electrochemical energy storage applications: state of the art, implementation, and synergy with metallic compounds for supercapacitor and battery electrodes, J. Power Sources 617 (2024) 235140, https://doi.org/10.1016/j.jpowsour.2024.235140.
[78] K. Silins, H. Baránková, L. Bardos, Protective amorphous carbon coatings on glass substrates, AIP Adv. 7 (11) (2017), https://doi.org/10.1063/1.5002091.
[79] C. Bommier, D. Mitlin, X. Ji, Internal structure – Na storage mechanisms – electrochemical performance relations in carbons, Prog. Mater. Sci. 97 (2018) 170–203, https://doi.org/10.1016/j.pmatsci.2018.04.006.
[80] M.G. Fyta, C. Mathioudakis, G. Kopidakis, P.C. Kelires, Structure, stability, and stress properties of amorphous and nanostructured carbon films, Thin Solid Films 482 (1) (2005) 56–62, https://doi.org/10.1016/j.tsf.2004.11.114.